


Science Paper

# Petrogenesis of the Early Paleogene North Island Syenite Complex, Seychelles

J. Gregory Shellnutt<sup>1</sup><sup>a</sup>, Tung-Yi Lee<sup>1</sup>, Yoshiyuki Iizuka<sup>2</sup>, Hao-Yang Lee<sup>2</sup>, Chi Thi Pham<sup>1</sup>, Kenshi Suga<sup>1</sup>

<sup>1</sup> Department of Earth Sciences, National Taiwan Normal University, <sup>2</sup> Institute of Earth Sciences, Academia Sinica

Keywords: Early Paleogene, A-type granite, Seychelles microcontinent, Deccan Traps, continental rift

<https://doi.org/10.2475/001c.94773>

## American Journal of Science

Vol. 324, 2024

The Early Paleogene (63.65 ± 0.52 Ma, 63.11 ± 0.45 Ma) North Island syenitic complex of the Seychelles microcontinent is composed principally of diorite (SiO<sub>2</sub> ≈ 57 wt%), syenite (SiO<sub>2</sub> = 61–65 wt%), and microsyenite (SiO<sub>2</sub> = ~70 wt%). The rocks are metaluminous, ferroan, and alkalic, and are compositionally similar to the A<sub>1</sub>-type granitoids. The trace element compositions of the syenitic rocks show minor spatial variability between the eastern (Congomet, Bernica) and western portions (Grand'Anse, Mt. Des Cèdres) of the island. The whole rock Sr-Nd (<sup>87</sup>Sr/<sup>86</sup>Sr<sub>i</sub> = 0.704095–0.707533; ε<sub>Nd</sub>(t) = +1.2–+1.9) and zircon Hf (ε<sub>Hf</sub>(t) = +2.1–+8.4) isotopes are indicative of a juvenile magma source. The low Th/Nb<sub>PM</sub> (0.3–1.5) and high Nb/U (30.9–109) ratios do not indicate a crustal origin of the rocks nor do they suggest crustal contamination was significant. Hydrous fractional crystallization modeling shows that a mafic alkaline parental magma can yield residual liquid compositions similar to the diorites and syenites under reducing conditions (ΔFMQ = –1) at a pressure of 0.3 GPa. However, feldspar accumulation likely occurred as some rocks have elevated Eu/Eu\* (>1.1) values. The emplacement of the North Island complex is contemporaneous with the eruption of the Deccan Traps and rifting of the Seychelles microcontinent from India. Rifting and magmatism was likely related to the passage of the Indian plate over the Réunion hotspot. The modeling results of the study demonstrate that crystallization pressure has an influence on whether basalt-derived A-type granitoids will evolve to metaluminous or peralkaline compositions.

## 1. INTRODUCTION

The term 'A-type' granite was introduced by Loiselle and Wones (1979) to describe granitic rocks that are found at rift zones and within stable continental blocks. Two compositionally distinct A-type granites were initially characterized. One sub-type is described as being derived by fractional crystallization of alkali basalt with minimal crustal interaction whereas the other sub-type is derived by interaction of crustal melts and alkali basalt. Eby (1990, 1992) classified the basalt-derived sub-type as A<sub>1</sub> and the crust-basalt-derived subtype as A<sub>2</sub>. Since the introduction of the A-type granite concept there has been significant interest in understanding the petrogenesis of each sub-type and constraining the petrological parameters under which these granites can develop as they are commonly associated with rare metal deposits and anorogenic tectonic settings including flood basalt provinces and orogenic collapse (Bonin, 2007; Černý, et al., 2005; Chakhmouradian & Zaitsev, 2012; Clemens et al., 1986; Collins et al., 1982; Dall'Agnolet al., 2012; Dostal, 2017; Eby, 1990; C. D. Frost & Frost,

1997; Landenberger & Collins, 1996; Patiño Douce, 1997). Although there is debate on the merit or usefulness of the 'A-type' concept, it has shown resilience and is still widely understood in spite of the ambiguity in its petrogenetic meaning (Bonin, 2007; C. D. Frost & Frost, 2011; Hogan et al., 1992).

The Seychelles microcontinent (~44,000 km<sup>2</sup>) is located at the northern end of the Mascarene plateau in the western Indian Ocean. It is a submerged fragment of continental crust that rifted from India during the Early Paleogene (Ashwal, 2019; Collier et al., 2008; Hammond et al., 2013; Torsvik et al., 2013). The outer islands of the Seychelles are mostly atolls with carbonate rocks and sandy shoals, but the inner islands are composed principally of A-type granitoids with subordinate mafic intrusive and silicic volcanic rocks (Ashwal et al., 2002; Dickin et al., 1986; Shellnutt et al., 2020; Weis & Deutsch, 1984). Nearly all of the granitic inner islands are Neoproterozoic (750–810 Ma) in age however the islands of Silhouette and North Island (Ile du Nord) are syenitic and Early Paleogene (60–65 Ma) in age (Dickin et al., 1986; Ganerød et al., 2011; Shellnutt et al., 2017,

<sup>a</sup> Corresponding author: jgshelln@ntnu.edu.tw

2020; Tucker et al., 2001). The Silhouette and North Island syenite complexes are considered to be petrogenetically associated with the eruption of the Deccan Traps and the passage of Indian plate over the Réunion hotspot (Devey & Stephens, 1992; Dickin et al., 1986; Gaina et al., 2015; Hammond et al., 2012; Owen-Smith et al., 2013). The island of Silhouette is composed of a volcanic unit (trachytic tuff) and a composite syenite and riebeckite granite ring complex (Baker, 1963; Dickin et al., 1986; Stephens, 1996). In contrast, North Island appears to be a single plutonic unit and therefore offers an opportunity to examine the formation of a 'self-contained' A-type granitoid associated with a flood basalt province.

North Island is low-lying and the smaller of the two Early Paleogene islands. It is composed of diorite, syenite, microsyenite, and microgranite and cross-cut by mafic dikes (Baker, 1963). The rocks are well exposed and readily accessible for collection. Although syenite predominates, in the southeast of the island (Congoment) there is a distinct region of intermixed diorite and syenite (Baker, 1963; Owen-Smith et al., 2013). Previous studies conclude that the North Island Complex (NIC) was derived by fractional crystallization of a mafic parental magma from the Réunion hotspot at low pressure (0.1 GPa). It is thought that the NIC and alkaline silicic rocks of Silhouette represent two eruptive centres of a single magmatic system (Dickin et al., 1986; Owen-Smith et al., 2013). However, zircon geochronology suggests that the rocks of North Island are slightly (~0.2 Ma to ~2.0 Ma) younger than the rocks of Silhouette and that they may be petrogenetically distinct magma systems (Ganerød et al., 2011; Shellnutt et al., 2017). Furthermore, the metaluminous nature of the syenitic rocks contrasts with the notion that they evolved at relatively low pressure as this tends to generate peralkaline compositions (C. D. Frost & Frost, 2011; Macdonald et al., 2011; Macdonald, 2012; Shellnutt et al., 2011, 2016; White et al., 2009). It is possible that contamination by crustal material (melt, fluids) may be responsible for the metaluminous nature of the syenites, but evidence for contamination is limited to non-existent (Owen-Smith et al., 2013). Therefore, an examination of the NIC can provide additional information on the nature of the youngest igneous rocks of the Seychelles microcontinent and on the petrogenesis of A<sub>1</sub>-type within-plate granitoids in general.

In this study, we present spot age zircon U-Pb geochronology and Hf isotopes, mineral chemistry, whole rock geochemistry, and whole rock Sr-Nd isotopes of diorites, syenites, and microsyenite from the North Island complex of the Seychelles. The data are used to constrain the tectonomagmatic evolution of the NIC within the context of Early Paleogene rifting of the Seychelles microcontinent from western India and the emplacement of the Deccan Traps. Moreover, we evaluate the importance of crystallization pressure in the formation of metaluminous A<sub>1</sub>-type granitoids.

## 2. GEOLOGICAL BACKGROUND

The Inner Islands of the Seychelles consist of three groups that are distinguished based on their geography, composition, and age (fig. 1). The majority of the Inner Islands are Precambrian in age and fall within two groups: the Mahé group (Mahé, St. Anne, Moyenne, Longue, Cerf, Anonyme, Sud-est, Mamelles, Concepcion, and Thérèse) and the Praslin group (Praslin, Cousine, Cousin, Aride, Curieuse, Les Soeurs, La Dique, Mariane, Recifs, and Fregate). The islands of the Mahé group are, granitic, grey in color, and have zircon U-Pb ages that range from 750–765 Ma. In comparison, the Praslin island group has a similar but more restricted age range (750–760 Ma) and they are composed of granites that are red to pink in color (Ashwal et al., 2002; Shellnutt et al., 2020; Tucker et al., 2001). An outlier of the Praslin group is Recifs as it yielded an older age of  $809 \pm 1.9$  Ma (Tucker et al., 2001). The origin of the Mahé and Praslin groups is debated as they are considered to be either related to an Andean-type active continental margin of Rodinia (Ashwal et al., 2002; Tucker et al., 2001) or an anorogenic/post-collisional setting (Shellnutt et al., 2020; Weis & Deutsch, 1984).

The third group of islands is composed of Silhouette and North Island (fig. 1B). North Island and Silhouette are the youngest islands and located at the western edge of the Inner Islands (Baker, 1963; Owen-Smith et al., 2013). The islands are composed primarily of greenish or buff colored syenitic rocks that yielded K-Ar, Ar-Ar, and U-Pb ages of 60–65 Ma (Baker & Miller, 1963; Dickin et al., 1986; Ganerød et al., 2011; Shellnutt et al., 2015, 2017; Stephens, 1996). There is a subordinate amount of mafic rocks on both islands (Devey & Stephens, 1992; Owen-Smith et al., 2013). Silhouette (20.1 km<sup>2</sup>) is located ~20 km NW of Mahé and is considered to be a ring complex of syenite and granite with two outcroppings of volcanic rocks along the easternmost portion of the island at Pointe Varreur-Pointe Ramsse and Pointe Zeng Zeng (Baker, 1963).

North Island is located five kilometres north of Silhouette and covers an area of 2.01 km<sup>2</sup> (fig. 2). The north and south regions of the island are rocky steep slopes whereas the eastern and western regions (Grand'Anse and Anse Bonnet Carret) are broad, calcareous, and sandy plateaux. The principal rock-type of North Island is buff grey syenite, but there is a small exposure of darker fayalite-biotite-bearing gabbro/diorite on the eastern side of the Congoment promontory (fig. 3A, B, C). Furthermore, there are also dark-colored veins, microgranular enclaves, and dikes of porphyritic microsyenite observed around Mt. des Cèdres and along the cross-island trail (fig. 3D). Seventeen samples were collected across North Island and include diorite, syenite, and a microsyenite vein (fig. 2).

## 3. PETROGRAPHY

### 3.1. DIORITE

The diorites (NI-001, NI-002) are coarse grained and granular and composed primarily of feldspar (~60 vol.%), clinopyroxene (~10 vol.%), fayalite (~10 vol.%), biotite (10–15

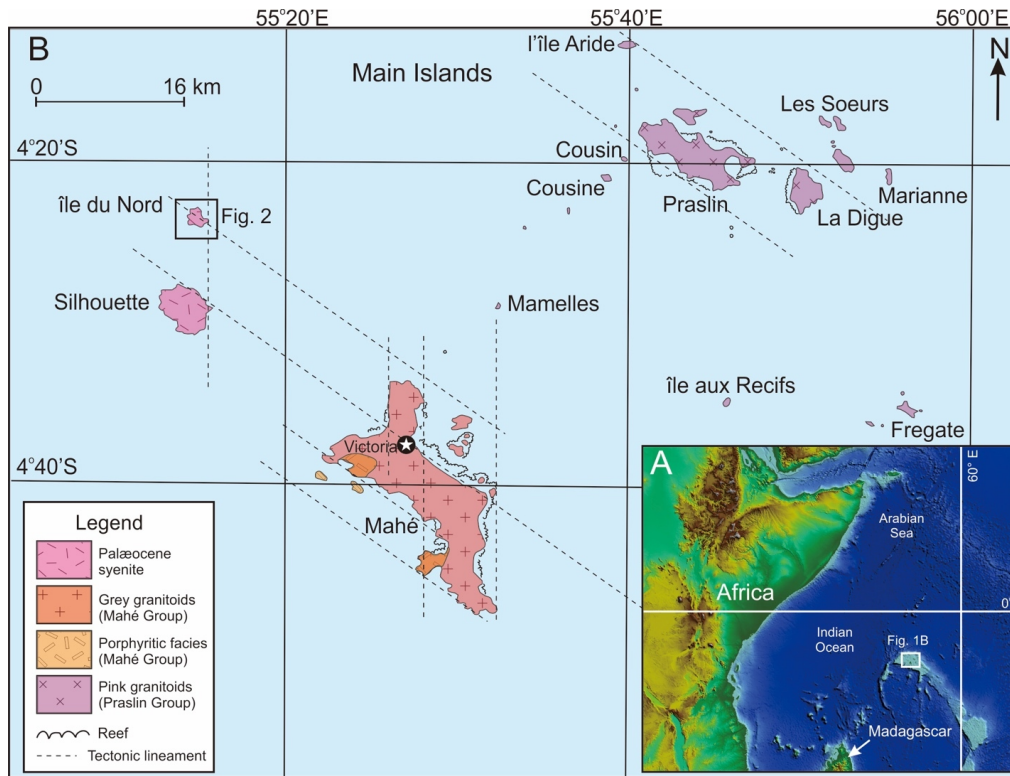


**Figure 1. (A) Location of the Seychelles microcontinent and (B) regional geological map of the inner islands of the Seychelles archipelago (modified from Baker, 1963). Dashed lines are lithospheric structures identified by Plummer and Belle (1995).**

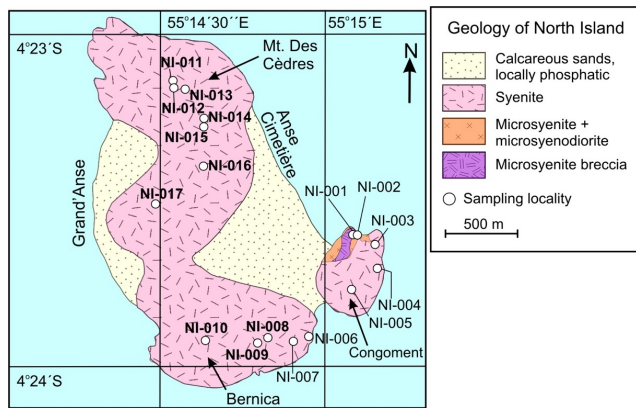


**Figure 2. Geological map of North Island and sample locations for this study (modified from Baker, 1963).**

vol.%), apatite (< 5 vol.%), and Fe-Ti oxide minerals (< 5 vol.%). There are accessory ( $\leq 1$  vol.%) amounts of zircon. Some feldspars have polysynthetic twinning whereas others have Carlsbad twinning. The twinning differences indicate that both plagioclase (oligoclase) and alkali feldspar (sanidine) are present in the diorites. Texturally, the plagioclase and alkali feldspar are euhedral to subhedral in shape and both feldspars are up to 1.5 cm long. The mafic minerals are primarily found within clusters interstitial to the feldspars where coarse grained euhedral biotite surrounds sub-rounded clinopyroxene and fayalite (fig. 4A, B). Euhedral acicular and hexagonal apatite and amorphous Fe-Ti oxide

minerals (ilmenite and magnetite) are also within the mafic mineral clusters.

### 3.2. SYENITE

The syenites are composed primarily of alkali feldspar (60–70 vol.%), clinopyroxene (5–15 vol.%), fayalite ( $\leq 10$  vol.%), biotite ( $\leq 10$  vol.%), amphibole ( $\leq 5$  vol.%), apatite (< 5 vol.%), and Fe-Ti oxide minerals (< 5 vol.%). There are accessory ( $\leq 1$  vol.%) amounts of quartz, orthopyroxene, plagioclase, titanite, and zircon. The rocks are fresh although some show evidence of low temperature deuteric alteration of feldspar, fayalite, and biotite. The modal abundance and textures have significant spatial variability. The syenites from southeastern North Island (NI-001–NI-008) are coarse grained and granular whereas the majority of rocks from the west and north (NI-009–NI-017) are medium grained and granular (fig. 4C–F). Moreover, the amount of fayalite decreases from east to west and the amount of amphibole increases from east to west. Generally, the alkali feldspars (albite, anorthoclase, sanidine) have irregular elongated shapes that are 0.1–1.5 cm long with a consertal texture and the majority has microperthite or perthite exsolution lamellae whereas a minority has Carlsbad twinning. In the coarse grained rocks, the mafic silicate and oxide minerals commonly form clusters that are  $\leq 1$  cm wide and interstitial to the alkali feldspars. The mineral clusters are composed of clinopyroxene, fayalite, euhedral biotite with zircon inclusions, Fe-Ti oxide minerals (ilmenite and magnetite), and euhedral apatite, with euhedral to sub-

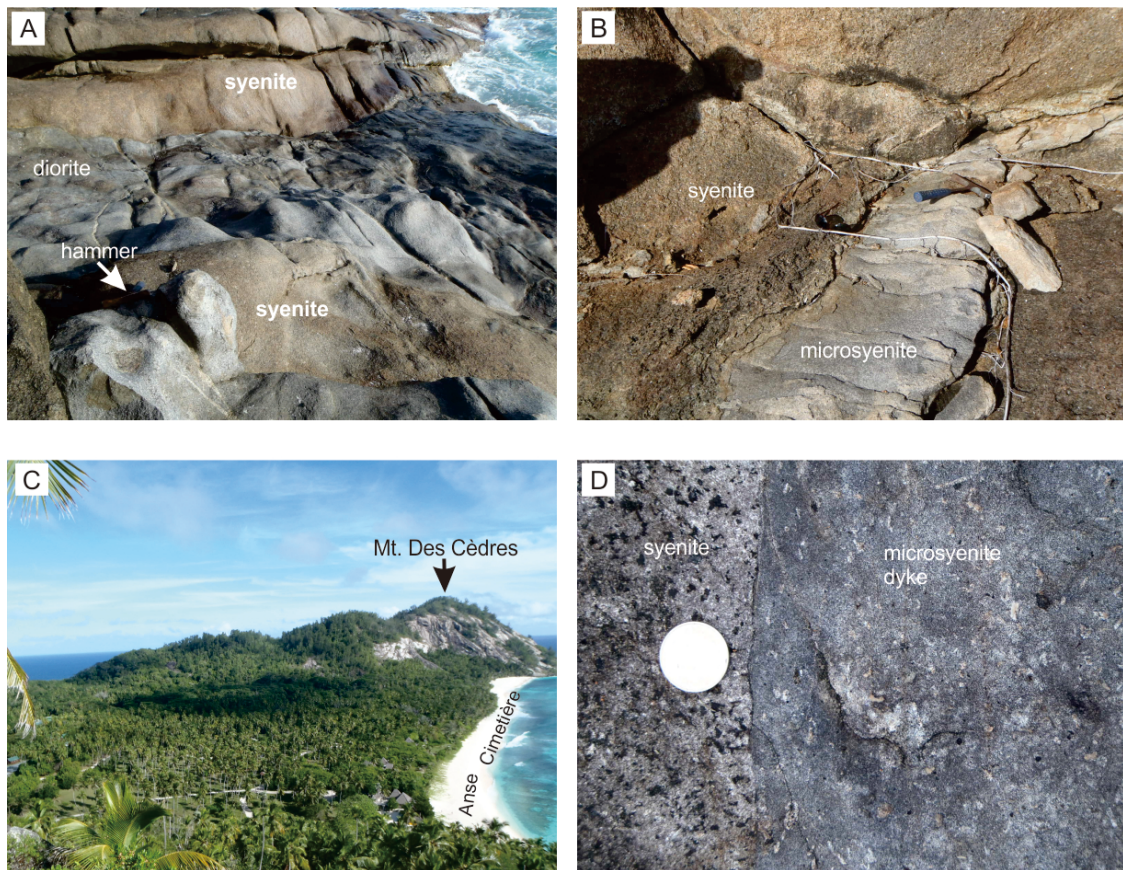


**Figure 3. Field photographs of North Island.**

(A) Compositional layering of the diorite and syenite from Congomont. (B) Microsyenite vein intruding the main body syenite. (C) Photograph of North Island looking north toward Mt. Des Cèdres from the top of Congomont. (D) Microsyenite dike intruding the main body syenite near Mt. Des Cèdres. The diameter of the coin is 24 mm.

hedral amphibole more commonly present in the western samples (fig. 4C, D). The medium grained rocks do not have large mineral clusters and instead tend to have single mafic minerals interstitial to the alkali feldspar (fig. 4E, F). The clinopyroxene is typically subhedral (rounded) with individual crystals up to ~5 mm long. The fayalite crystals are sub-round to equant in shape and up to ~3 mm wide. Fayalite is identified by its high relief and the presence of iddingsite around the crystal boundaries as well as in mineral fractures. Within the mineral cluster it is common for biotite, Fe-Ti oxide minerals, and apatite to be associated whereas clinopyroxene or fayalite are often but not always within the cluster. Quartz and plagioclase, identified by polysynthetic twinning, are rare, but, if present, are small (< 0.5 mm wide) and interstitial to the alkali feldspar. Titanite and zircon are not abundant and identified based on their relief, color, and birefringence.

### 3.3. MICROSYENITE

The microsyenite (NI-004V) is medium to fine grained and granular. It is composed of alkali feldspar (70–75 vol.%), quartz (~10 vol.%), amphibole (5–10 vol.%), biotite (≤ 5 vol.%), clinopyroxene (< 5 vol.%), and Fe-Ti oxide minerals (≤ 5 vol.%). There are accessory (< 1 vol.%) amounts of zir-

con and apatite. The rock is fresh although many of the feldspar crystals show minor saussurite alteration. The alkali feldspars are euhedral to subhedral and with the majority (60–70%) having perthite exsolution texture and a minority (30–40%) showing cross-hatched twinning. All other minerals are interstitial to the alkali feldspar. The mafic minerals do not cluster and are randomly distributed. The amphibole and clinopyroxene are distinguished by their cleavage, but have similar size and textures (subhedral to euhedral). The biotite is euhedral and contains zircon inclusions. Fe-Ti oxide minerals are spatially associated with the mafic minerals and typically have euhedral to subhedral shapes.

## 4. ANALYTICAL METHODS

### 4.1. ELECTRON PROBE MICRO-ANALYZER

The mineralogical investigation was carried out by a field emission electron microprobe (JEOL EPMA JXA-8500F) equipped with five wave-length dispersive spectrometers (WDS). Each rock specimen was sliced to a 1-inch diameter size and mounted into epoxy resin, and then polished. Secondary- and back-scattered electron images were used to guide the analysis on targeted positions of minerals. A 2 μm

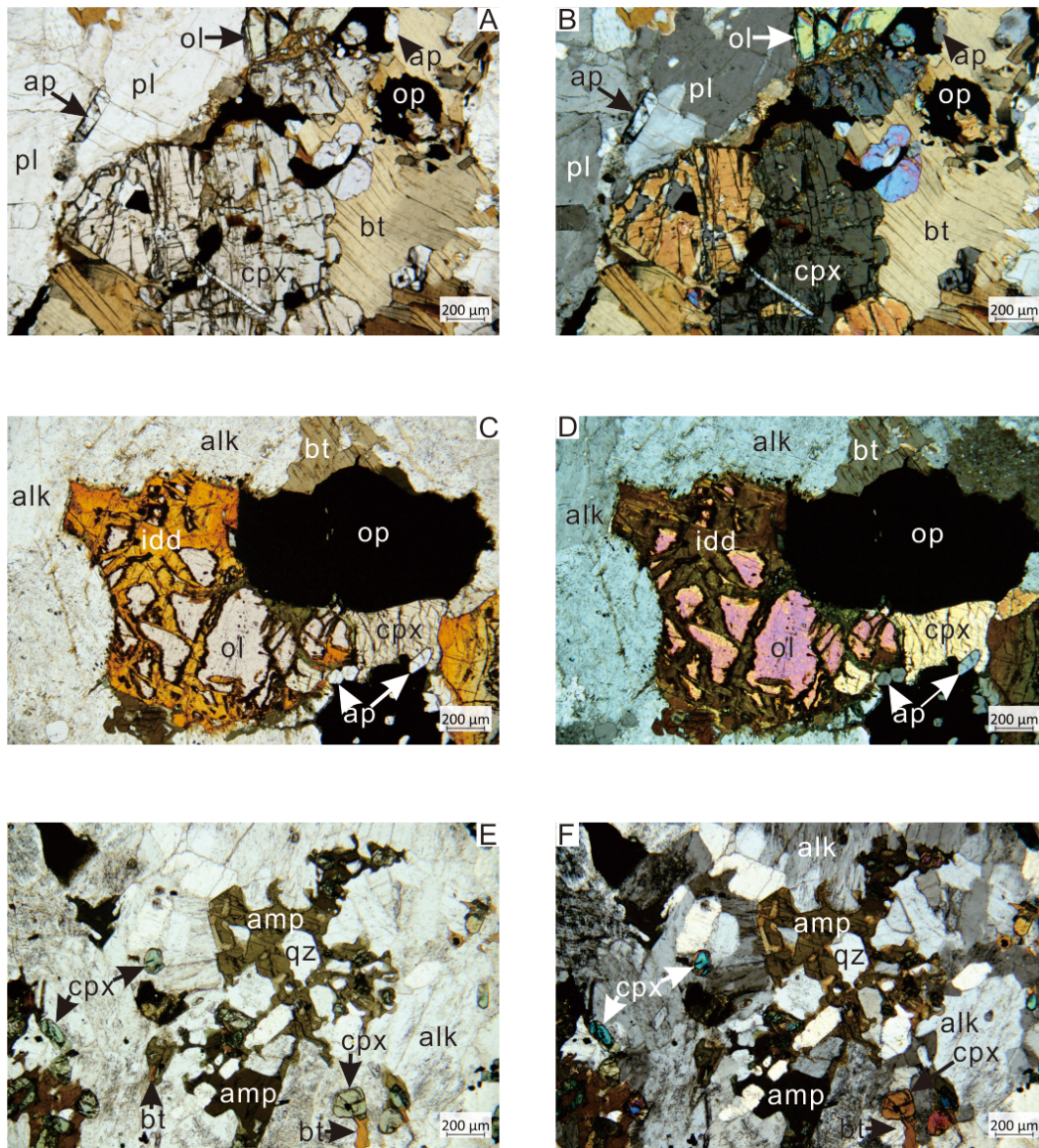


**Figure 4. Photomicrographs of the rocks of the North Island complex.**

(A) Plane polarized light and (B) crossed polarized photos of the diorite (NI-001). (C) Plane polarized light and (D) crossed polarized photos of the coarse grained syenite (NI-004). (E) Plane polarized light and (F) crossed polarized photos of the medium grained syenite (NI-012). Symbols: alk = alkali feldspar, bt = biotite, pl = plagioclase, op = opaque, amp = amphibole, ol = olivine (fayalite), cpx = clinopyroxene, idd = iddingsite, ap = apatite.

defocused beam was operated for quantitative analysis at an acceleration voltage of 12 kV with a beam current of 6 nA. The measured X-ray intensities were corrected by ZAF-oxide method using the standard calibration of synthetic and natural chemical-known standards with various diffracting crystals. They include: wollastonite for Si- $K\alpha$ , with TAP crystal, rutile for Ti- $K\alpha$  with PET crystal, corundum for Al- $K\alpha$  (TAP), chromium oxide for Cr- $K\alpha$  (PET), hematite for Fe- $K\alpha$  with LiF crystal, manganese oxide for Mn- $K\alpha$  (PET), periclase for Mg- $K\alpha$  (TAP), nickel oxide for Ni- $K\alpha$  (LiF), zinc oxide for Zn- $K\alpha$  (LiF), wollastonite for Ca- $K\alpha$  (PET), albite for Na- $K\alpha$  (TAP), sanidine for K- $K\alpha$  (PET), fluorite for F- $K\alpha$  (TAP), and apatite for P- $K\alpha$  (PET). Peak counting times for F was 20s, and others were 10s, respectively. The measured values of the reference standards were within 1%

of accepted values. The mineral chemistry results are presented in supplementary table S1 (<https://doi.org/10.17632/8mkngdftfp.2>).

#### 4.2. LA-ICP-MS/MS GEOCHRONOLOGY

The analytical method is summarized in table S2, following the reporting template of Horstwood et al. (2016), and detailed in Supplementary Materials, Methods. Zircon U-Pb dating was carried out using an Agilent 8900 Triple Quadrupole ICP-MS (ICP-MS/MS; Agilent, Santa Clara, CA, US) coupled to a Teledyne CETAC Analyte Excite Plus laser-ablation system (Teledyne CETAC, Omaha, NE, US), that utilizes a 193 nm ArF excimer laser, at the Department of Earth Sciences, National Taiwan Normal University. The U-

Th-Pb isotope analysis was conducted in MS/MS mode; the isobaric interference of  $^{204}\text{Hg}$  on  $^{204}\text{Pb}$  was minimized using a gas-phase charge transfer reaction with  $\text{NH}_3$  reaction gas in the reaction cell (Woods, 2017). The spot size of the laser used in this study is 25  $\mu\text{m}$  in diameter. 91500 zircon and NIST SRM 610 glass reference materials were used for an external calibration of U/Pb and Pb/Pb isotope ratios, respectively. Data reduction was conducted off-line, using an in-house excel spreadsheet for U-Th-Pb age data reduction (Hattori et al., 2017; Sakata et al., 2014). Using the Hg-corrected  $^{204}\text{Pb}$ , a correction for common Pb was made on the basis of the  $^{204}\text{Pb}$  method (Stern, 1997) and the model for the common Pb compositions (Stacey & Kramers, 1975).

During the analyses, Plešovice (Sláma et al., 2008) and AS3 (Paces & Miller, 1993) zircons were used as secondary standards for data quality assessment (Supplementary Materials, Data). The  $^{206}\text{Pb}/^{238}\text{U}$  age weighted-mean age for Plešovice zircon determined in this study yielded  $333.2 \pm 4.7$  Ma ( $n = 4$ ; MSWD = 1.3) and is consistent with the age of  $337.13 \pm 0.37$  Ma reported by Sláma et al. (2008). The  $^{207}\text{Pb}/^{206}\text{Pb}$  weighted-mean age for AS3 zircon determined in this study yielded  $1094 \pm 39$  Ma ( $n = 4$ ; MSWD = 0.59) and is consistent with the age of  $1099.1 \pm 0.5$  Ma reported by Paces and Miller (1993). The data was plotted using Isoplot 3.75 (Ludwig, 2012) and the results can be found in table S3.

#### 4.3. ZIRCON HF ISOTOPES

Zircon Hf isotope analyses were carried out on the zircon crystals analyzed for U-Pb dating reported by Shellnutt et al. (2017). A Photon Machines Analyte G2 laser-ablation microprobe attached to a Nu Plasma HR multi-collector ICP-MS was used at the Institute of Earth Sciences, Academia Sinica in Taipei. The Nu Plasma HR MC-ICP-MS features a unique geometry with a fixed detector array of 12 Faraday cups and 3 ion counters. For this study, masses 172, 175, 176, 177, 178, 179 and 180 were simultaneously analyzed. Data were considered for isobaric interferences and normalized to  $^{179}\text{Hf}/^{177}\text{Hf} = 0.7325$ , using an exponential correction for mass bias. Isobaric interferences of  $^{176}\text{Lu}$  and  $^{176}\text{Yb}$  on  $^{176}\text{Hf}$  were corrected by measuring the intensities of the interference-free  $^{175}\text{Lu}$  and  $^{172}\text{Yb}$  isotopes and using appropriate  $^{176}\text{Lu}/^{175}\text{Lu}$  and  $^{176}\text{Yb}/^{172}\text{Yb}$  ratios to calculate  $^{176}\text{Lu}$  and  $^{176}\text{Yb}$  values. In the method of Griffin et al. (2000) it is assumed that  $f\text{Hf} = f\text{Yb} = f\text{Lu}$  ( $f$  is the mass fractionation coefficient) and the mass bias obtained for Hf is also applied to the Yb and Lu mass bias correction. Griffin et al. (2000) tested this correction method by analyzing solutions of JMC475 spiked with Yb and JMC475 spiked with Lu. The 'true' values for  $^{172}\text{Yb}/^{176}\text{Yb}$  and  $^{175}\text{Lu}/^{176}\text{Lu}$  were adjusted to give the 'true'  $^{176}\text{Hf}/^{177}\text{Hf}$  of JMC475. The Yb and Lu isotopic compositions derived from the solution analyses were then used to correct the laser analyses. The instrumental conditions and data acquisition are similar to Griffin et al. (2000). The accuracy and precision of the method are shown by the analyses of reference zircons (Mud Tank, Plešovice, 91500, and TEMORA) and the accuracy of the correction procedure was demonstrated for  $^{176}\text{Yb}/^{177}\text{Hf} \leq 0.1$  and  $^{176}\text{Lu}/^{177}\text{Hf} \leq 0.10$ , encompassing

the vast majority of typical zircon ( $^{176}\text{Yb}/^{177}\text{Hf} \leq 0.1$  and  $^{176}\text{Lu}/^{177}\text{Hf} \leq 0.002$ ; Belousova et al., 2002; Griffin et al., 2004, 2006) and the zircon samples in this study ( $^{176}\text{Yb}/^{177}\text{Hf} \leq 0.1$  and  $^{176}\text{Lu}/^{177}\text{Hf} \leq 0.0030$ ).

The Photon Machines Analyte G2 excimer laser ablation system delivers a beam of 193 nm UV light with a wide range of fluences (<1 to 40  $\text{J}/\text{cm}^2$ ). Most analyses were carried out with a beam diameter of 50  $\mu\text{m}$ , 8 Hz repetition rate, and energy of  $\sim 8\text{--}9$   $\text{J}/\text{cm}^2$ . This resulted in total Hf signals of up to  $\sim 10$  V, depending on the precise conditions and Hf contents. Analyzing times were  $\sim 2$  minutes including 30 seconds of the background noise and  $\sim 80$  seconds of the sample ablation. The He carrier gas of  $\sim 0.9$  L/min (MFC1 =  $\sim 0.7$  L/min and MFC2 =  $\sim 0.2$  L/min) transported the ablated sample from the laser-ablation cell via a mixing chamber where it was mixed with Ar of  $\sim 0.7$  L/min prior to entering the ICP-MS torch. The He gas could substantially reduce the deposition of ablated material onto the sample surface and greatly improve transport efficiency, and thus increase the signal intensities. Laser-ablation analyses were carried out using time-resolved analysis (TRA) software, in which the signal for each mass and ratio is displayed as a function of time during the analysis. This allows the more stable portions of the ablation to be selected for analysis, before the data are processed to yield the final results. Typical within-run precision ( $1\sigma$ ) on the analysis of  $^{176}\text{Hf}/^{177}\text{Hf}$  is better than  $\pm 0.000030$ , equivalent to an uncertainty of  $\sim 1$  epsilon unit. International zircon standard Mud Tank was used as the primary external reference material to monitor the condition of facilities and Plešovice, 91500, and TEMORA served as the secondary external reference materials for data quality control. They have long-term average  $^{176}\text{Hf}/^{177}\text{Hf}$  values of  $0.282496 \pm 29$  ( $2\sigma$ ,  $n = 636$ ),  $0.282483 \pm 21$  ( $2\sigma$ ,  $n = 84$ ),  $0.282314 \pm 23$  ( $2\sigma$ ,  $n = 40$ ), and  $0.282689 \pm 30$  ( $2\sigma$ ,  $n = 42$ ), respectively, all in accordance with those of  $0.282504 \pm 44$ ,  $0.282482 \pm 13$ ,  $0.282307 \pm 31$ ,  $0.282680 \pm 31$  reported in Woodhead and Hergt (2005), Wu et al. (2006), and Sláma et al. (2008). The  $\epsilon_{\text{Hf}}(t)$  values (parts in  $10^4$  deviation of initial  $^{176}\text{Hf}/^{177}\text{Hf}$  isotopic ratios between the sample and the chondritic uniform reservoir), the depleted mantle model ages ( $T_{\text{DM}}$ ), with the assumption that the protolith of the zircon's host magma had the average continental crustal  $^{176}\text{Lu}/^{177}\text{Hf}$  ratio of 0.015, were calculated after Griffin et al. (2004) using the  $^{176}\text{Lu}$ - $^{177}\text{Hf}$  decay constant of  $1.867 \times 10^{-11}$  (Söderlund et al., 2004), and the chondritic values of  $^{176}\text{Hf}/^{177}\text{Hf}$  (0.282772) and  $^{176}\text{Lu}/^{177}\text{Hf}$  (0.0332) from Blichert-Toft and Albarède (1997). The results are presented in table S4.

#### 4.4. X-RAY FLUORESCENCE SPECTROMETRY

Rock samples were cut into small pieces using a diamond-bonded steel saw and were then crushed in a steel jaw crusher. The crusher was rinsed and cleaned with de-ionized water after each sample was processed. The crushed samples were pulverized to 200 mesh in an agate mill. After drying the samples at 105  $^{\circ}\text{C}$  they were heated to 900  $^{\circ}\text{C}$  to determine loss on ignition (LOI). The masses of each sample were measured after 105  $^{\circ}\text{C}$  and 900  $^{\circ}\text{C}$ . 6.0000

$\pm 0.0005$  grams of lithium metaborate (49.75%  $\text{Li}_2\text{B}_4\text{O}_7$ , 49.75%  $\text{LiBO}_2$ , and 0.5%  $\text{LiBr}$ ) was mixed with  $0.6000 \pm 0.0005$  grams of each sample and fused to produce a glass disc using a Claisse M4 fluxer. The major oxide concentrations were measured by WD-XRFS using a PANalytical Axios mAX spectrometer at National Taiwan Normal University in Taipei. The measured major elemental data of United States Geological Survey standard reference materials BIR-1 and SDC-1 are reported in table S5.

#### 4.5. WHOLE ROCK TRACE ELEMENTS

Trace elements were measured using an Agilent 7500cx inductively coupled plasma mass spectrometer (ICP-MS) at the Institute of Earth Sciences, Academia Sinica, Taipei. Approximately 40 mg of fused glass bead from each sample was dissolved using super-pure HF and  $\text{HNO}_3$  (1:1) mixture in screw-top Teflon beakers for  $> 12$  h at  $\sim 140$  °C, followed by evaporation to dryness, and refluxed in 2 ml  $\text{HNO}_3$  (1:2) for  $> 12$  h at  $\sim 140$  °C. Then samples were diluted using 2%  $\text{HNO}_3$  and 10 ppb Rh and Bi spike was added for the internal standard. The spiked solution was diluted with 2%  $\text{HNO}_3$  to a sample/solution weight ratio of 1:1500. United States Geological Survey standard reference materials analyzed for trace elements are BCR-2, BHVO-2, and DNC-1. The accuracy of the measured standard reference material is better than  $\pm 5$  % for all elements (table S5).

#### 4.6. THERMAL IONIZATION MASS SPECTROMETRY

Strontium isotopes were measured at two different laboratories. Samples NI-002 and NI-003 were measured at Activation Laboratories, Ancaster, Ontario. The samples were dissolved using HF+ $\text{HNO}_3$  and Sr was separated following the procedures of Creaser et al. (2004) and Holmden et al. (1997). Isotopic analysis was carried out using a multi-collector inductively coupled plasma mass spectrometer (MC-ICP-MS). All analyses are presented relative to a value of 0.710245 for the SRM987 Sr isotopic standard. The remaining samples (NI-004, NI-009, NI-010, NI-016) were analyzed at Academia Sinica, Institute of Earth Sciences, Taipei, Taiwan using a Finnigan MAT-262 thermal ionization mass spectrometer (TIMS). Each sample was weighed (75–100 mg) and loaded into a Teflon beaker, dissolved by a mixture of HF and  $\text{HNO}_3$  (50 drops of each acid), and heated on a hotplate ( $\sim 100$  °C) for 48 hours. The solution was dried and another 2 mL 6N HCl was added to redissolve the samples. This step was done twice in order to ensure complete dissolution. After drying, another 2 ml 1N HCl was added to the beaker and followed by centrifuging for 10 minutes. The supernatant was transferred to a new beaker. This step was repeated until all of the samples were digested. The samples were then added to columns (2.5 ml 100–200 mesh Bio-Rad AG 50W-X8 cation exchange resin) to separate Sr and rare earth elements (REEs). The columns were equilibrated with 2N HCl before loading the samples. After the sample solution was loaded into the column, 3 mL 2N HCl was added to the beaker to wash out the remaining sample and then loaded into the column, followed by 18 mL 2N HCl to rinse. Strontium was collected following the addition

of 12 mL 2N HCl in a new beaker. Another 3 mL 2 N HCl was added and discarded. The rare earth elements were collected following 13 mL 6N HCl in a new beaker. The solutions of Sr and REE were dried and 1 mL 2N HCl was added to the Sr beaker and 0.1mL milliQ water to the REE beaker.

The strontium column (1 mL 100–200 mesh Bio-Rad AG 50W-X8 resin) was used to further purify the Sr. The columns were first equilibrated using 2N HCl. The Sr solution separated from the initial column was loaded into the Sr column. One mL of 2N HCl was added into the beaker to wash out the remaining sample and loaded into the column. The beaker-wash out step was repeated twice. Another 4 mL 2N HCl was added into the column. Strontium was collected following 10 mL 2N HCl and dried after the collection. One drop each of HCl and  $\text{HNO}_3$  was added to the dried sample and then repeated three times. Rare earth elements were separated using polyethylene columns with a 5 ml resin bed of AG 50W-X8, 200–400 mesh. Neodymium was separated from other REEs using an Ln resin as a cation exchange medium. The samples were loaded on to Re filaments with one drop of  $\text{H}_3\text{PO}_4$  and then dried with a 0.8–1.0 mA current. The  $^{143}\text{Nd}/^{144}\text{Nd}$  ratios were normalized to  $^{146}\text{Nd}/^{144}\text{Nd} = 0.7219$  and  $^{87}\text{Sr}/^{86}\text{Sr}$  ratios to  $^{86}\text{Sr}/^{88}\text{Sr} = 0.1194$ . The Sr isotopic ratios were measured using a Finnigan MAT-262 thermal ionization mass spectrometer (TIMS) whereas the Nd isotopic ratios were measured using a Finnigan Triton TIMS in the Mass Spectrometry Laboratory, Institute of Earth Sciences, Academia Sinica, Taipei. The  $2\sigma_m$  values for all samples are less than or equal to 0.000028 for  $^{87}\text{Sr}/^{86}\text{Sr}$  and less than or equal to 0.000007 for  $^{143}\text{Nd}/^{144}\text{Nd}$  (table S6). The measured isotope ratio for JMC Nd standard is  $0.511813 \pm 0.000010$  ( $2\sigma_m$ ) and NBS987-Sr is  $0.710248 \pm 0.00001$  ( $2\sigma_m$ ).

## 5. RESULTS

### 5.1. MINERAL CHEMISTRY

#### 5.1.1. OLIVINE

Fayalite was analyzed from sample NI-003 and it has a nearly pure end-member composition with a narrow range of  $\text{Fa}_{92.4-94.5}$ . Silica ranges from  $\sim 29.5$  to  $\sim 30.8$  wt.% with MnO from  $\sim 3.1$  to  $\sim 3.9$  wt.% and MgO from  $\sim 2.1$  to  $\sim 2.9$  wt.%.

#### 5.1.2. ORTHOPYROXENE

Orthopyroxene (ferrosilite) is not abundant ( $< 1$  vol.%) in the North Island Complex and was analyzed from sample NI-009. The crystals have a compositional range of  $\text{Wo}_{1.5-1.8}\text{En}_{19.7-21.3}\text{Fs}_{78.9-76.9}$  and Mg# of 20.0 and 21.7. The concentrations of  $\text{Al}_2\text{O}_3$  (0.14–0.16 wt%),  $\text{TiO}_2$  ( $< 0.1$  wt%) and CaO ( $\leq 0.7$  wt%) are low. It is possible that the ferrosilite is a secondary mineral as the major oxide sum totals tend to be low (96–98 wt%).

### 5.1.3. CLINOPYROXENE

The clinopyroxene classify as diopside-hedenbergite within the pyroxene quadrilateral and have compositions of  $Wo_{44.8-50.0}En_{13.9-32.8}Fs_{20.6-40.6}$ . The minor elements such as  $TiO_2$  (0.14–0.64 wt.%),  $Al_2O_3$  (0.65–1.04 wt.%), MnO (0.44–1.11 wt.%), and  $Na_2O$  (0.34–0.70 wt.%) are similar across all samples. The crystals in the diorites are MgO-rich ( $Wo_{45.5-50.0}En_{22.8-32.8}Fs_{20.6-28.0}$ ) compared to those from the syenites ( $Wo_{44.8-47.3}En_{13.9-23.8}Fs_{30.8-40.6}$ ).

### 5.1.4. AMPHIBOLE

The amphiboles from the North Island syenites are calcic and classify ( $Ca_B \geq 1.5$ ;  $(Na+K)_A \geq 0.50$ ;  $Ti < 0.5$ ;  $Mg/(Mg+Fe^{2+}) < 0.5$ ) as hastingsite-ferropargasite (Leake et al., 1997). The cation mineral formulae were calculated using PROBE-AMPH of Tindle and Webb (1994). The  $TiO_2$  (1.51–4.27 wt%),  $Al_2O_3$  (6.70–10.08 wt%), TFeO (26.51–31.14 wt%), MgO (2.75–4.30 wt%), CaO (9.94–10.97 wt%),  $Na_2O$  (2.05–3.12 wt%), and  $K_2O$  (0.79–1.59 wt%) concentrations are variable. However, the amphiboles within the syenites from eastern (NI-007) North Island are generally more magnesian than those from western (NI-009, NI-014, NI-016) North Island.

### 5.1.5. BIOTITE

The biotite crystals have magmatic compositions (Nachit et al., 2005) and show compositional variability from higher MgO to lower MgO across different rock types. The diorites have biotite with Fe/Fe+Mg values of 0.64 to 0.75 whereas the biotites from the syenites have values of 0.79 to 0.97. Furthermore, the  $TiO_2$  ( $TiO_2 = 4.97-7.09$  wt.%) concentrations of the biotites from the diorites are generally higher than the biotites ( $TiO_2 = 2.33-5.79$  wt.%) from the syenites. The  $Al_2O_3$  (diorite = 12.63–13.93 wt.%; syenite = 9.88–13.11 wt.%) and  $K_2O$  (diorite = 8.67–9.75 wt.%; syenite = 7.62–9.38 wt.%) concentrations are similar between the two rock types. The biotite mineral formulae were calculated using the method of Tindle and Webb (1990).

### 5.1.6. FELDSPAR

Alkali feldspars are the most abundant phenocrysts in the syenites whereas plagioclase feldspar is more common in the diorites. The diorites contain sanidine-anorthoclase ( $An_{2.0-6.7}Ab_{28.2-61.3}Or_{32.0-69.0}$ ) and andesine-oligoclase ( $An_{8.8-29.2}Ab_{68.1-89.4}Or_{1.8-5.0}$ ). The syenites are composed of perthitic feldspar with near end-member albite ( $Ab > 90$ ) and orthoclase ( $Or > 90$ ) compositions and anorthoclase-sanidine ( $An_{1.2-6.1}Ab_{31.4-76.5}Or_{19.6-67.2}$ ).

### 5.1.7. TITANITE

Titanite was analyzed in sample NI-014 and the mineral formulae were calculated on the basis of four Si. The sum totals range from 94.32 wt.% to 98.23 wt.% suggesting there is an appreciable amount of volatile (OH-, Cl-, F-) and/or trace elements in the crystals. The total iron content

(2.22–3.32 wt.%), as expressed as  $Fe_2O_3$ ,  $TiO_2$  (34.08–36.24 wt.%), and CaO (26.13–27.95 wt.%) do not vary significantly.

### 5.1.8. ILMENITE

The total FeO contents range from 41.38–48.68 wt.% whereas  $TiO_2$  ranges from 49.18–53.82 wt.%. The ferrous and ferric iron was calculated by charge balance and all samples have  $Fe^{3+}/Fe^{2+}$  ratios of  $\leq 0.11$ . The MnO concentration ranges from 1.79–6.37 wt.% whereas the MgO is  $\leq 0.25$  wt.%. The ilmenite crystals from each sample are compositionally similar.

### 5.1.9. MAGNETITE

Magnetite is less abundant than ilmenite in the rocks and has significantly more chemical variability than the ilmenite. The total FeO contents range from 72.76–92.50 wt.% whereas  $TiO_2$  ranges from 0.66–17.70 wt.%. Ferric and ferrous iron are calculated by charge balance and all samples have  $Fe^{3+}/Fe^{2+}$  ratios from 0.63 to 1.82. The MnO concentration ranges from below detection limit to 1.91 wt.%. There is no observable difference between the magnetites from across the samples.

## 5.2. ZIRCON U-PB GEOCHRONOLOGY

Twenty-one (24 spots) individual zircon crystals were analyzed from sample NI-014 (table S3). The zircons range in length from ~100  $\mu m$  to ~500  $\mu m$  and have euhedral to sub-hedral shapes, but many crystals are fragmented (fig. S1). Some zircons exhibit oscillatory zoning (e.g., 1, 9, 12, 14, 15, 16-17, 19, 20-21, 23-24) and lack core-rim structures, but there are a few crystals that appear to have irregular core-rim structure (e.g., 2, 6, 8, 10, 11, 18) whereas others (e.g., 3, 4, 5, 7, 13, 22) have textures similar to post-magmatic recrystallized zircon (cf., Corfu et al., 2003). The targeted spot locations were regions without structure and have oscillatory zoning. The total range of the  $^{238}U/^{206}Pb$  ages is from  $60.0 \pm 1.3$  Ma to  $95.9 \pm 6.6$  Ma. Measured uncertainties are reported at the  $2\sigma$  level for each spot analysis (table S3). The Th/U ratios range from 0.05 to 2.15 with the oldest zircon having the lowest value. Our results show that there are three age populations of zircons. The youngest zircon has a  $^{238}U/^{206}Pb$  age of  $60.0 \pm 1.3$  Ma which is anomalously young relative to the main population of zircons (fig. 5A). The main population (17 zircons) has  $^{238}U/^{206}Pb$  ages from  $61.2 \pm 1.2$  Ma to  $65.0 \pm 1.4$  Ma. The oldest zircons have ages from  $68.0 \pm 1.1$  Ma to  $95.9 \pm 6.6$  Ma which we consider to be inherited, in part due to their post-magmatic recrystallization textures, and are not included in the crystallization age calculation. If all zircons except those considered to be inherited are used to calculate the weighted-mean age ( $63.40 \pm 0.67$  Ma) then the resultant age has a high MSWD (3.7) and a probability of confidence of 0. Furthermore, a Concordia age cannot be determined. If only the zircons of the main population are considered than the weighted-mean  $^{238}U/^{206}Pb$  age  $63.65 \pm 0.52$  Ma (MSWD = 2.0). The Concordia age of the main population is  $63.64 \pm$



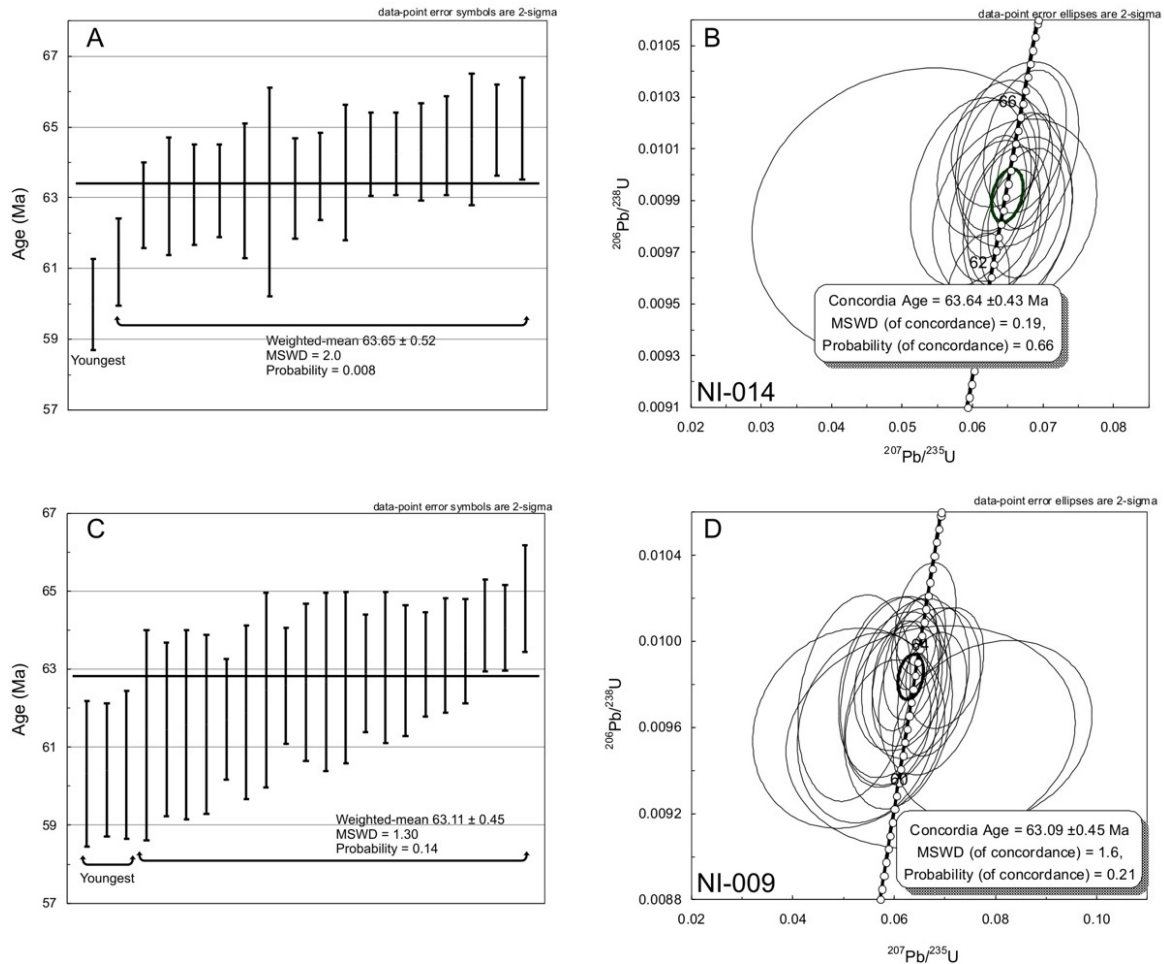


**Figure 5. Results of spot age zircon U-Th-Pb geochronology of syenitic rocks from North Island complex.**

(A)  $^{206}\text{Pb}/^{238}\text{U}$  ages with the weighted-mean age of the main zircon population from sample NI-014 (see text for details). (B) Concordia plot of the main population zircons from sample NI-014. (C)  $^{206}\text{Pb}/^{238}\text{U}$  ages with the weighted-mean age of the main zircon population from sample NI-009 (see text for details). (D) Concordia plot of the main population zircons from sample NI-009.

0.43 Ma (MSWD = 0.19) (fig. 5B). Consequently, we consider the main population zircons to be representative of the crystallization age of the rock.

Twenty-four zircon crystals were analyzed from sample NI-009 (table S3). The zircons range in length from  $\sim 75\ \mu\text{m}$  to  $\sim 150\ \mu\text{m}$  and have euhedral to subhedral shapes (fig. S2). The zircons exhibit oscillatory zoning and very few have core-rim structures. The range of the  $^{238}\text{U}/^{206}\text{Pb}$  ages is from  $60.3 \pm 1.9\ \text{Ma}$  to  $68.8 \pm 1.2\ \text{Ma}$ . Measured uncertainties are reported at the  $2\sigma$  level for each spot analysis (table S3). The Th/U ratios range from 0.41 to 1.93 and within the range of igneous zircons (Hoskin & Schaltegger, 2003). Similar to sample NI-014, three populations are identified. The three youngest zircons are  $60.3 \pm 1.9\ \text{Ma}$ ,  $60.5 \pm 1.9\ \text{Ma}$ , and  $60.4 \pm 1.7\ \text{Ma}$  and are similar to the youngest zircon from sample NI-014. The main population (20 zircons) range in age from  $61.3 \pm 2.7\ \text{Ma}$  to  $64.2 \pm 1.4\ \text{Ma}$  whereas the oldest zircon is considered to be inherited ( $68.8 \pm 1.2\ \text{Ma}$ ). If all zircons except those considered to be inherited are used to calculate the weighted-mean age ( $62.92 \pm 0.52\ \text{Ma}$ ) then the resultant age has a high MSWD (2.1), low probability of confidence of 0.002, and a Concordia age can-

not be calculated (fig. 5C). In comparison, the weighted-mean  $^{238}\text{U}/^{206}\text{Pb}$  age of the main population is  $63.11 \pm 0.45\ \text{Ma}$  (MSWD = 1.3) and the Concordia age is  $63.09 \pm 0.45\ \text{Ma}$  (MSWD = 1.76) (fig. 5D). We consider the main population zircon group to be representative of the crystallization age of the rock.

The crystallization ages ( $63.65 \pm 0.52\ \text{Ma}$  and  $63.11 \pm 0.45\ \text{Ma}$ ) of NI-014 and NI-009 and their uncertainty fall within the range of the zircon U-Pb ID-TIMS ages ( $63.28 \pm 0.08$ ,  $63.31 \pm 0.11$ ,  $63.20 \pm 0.12\ \text{Ma}$ ,  $63.24 \pm 0.14$ ) reported by Ganerød et al. (2011) for North Island and are older than the ages ( $60.6 \pm 0.6\ \text{Ma}$  to  $61.0 \pm 0.8\ \text{Ma}$ ) reported by Shellnutt et al. (2017). The discrepancy between the younger and older spot ages could be related to the methods used (i.e., LA-ICP-MS vs. LA-ICP-MS/MS). However, the identification of younger zircons in this study suggests that the magmas may have crystallized over a prolonged period of time (i.e., 60–63 Ma).

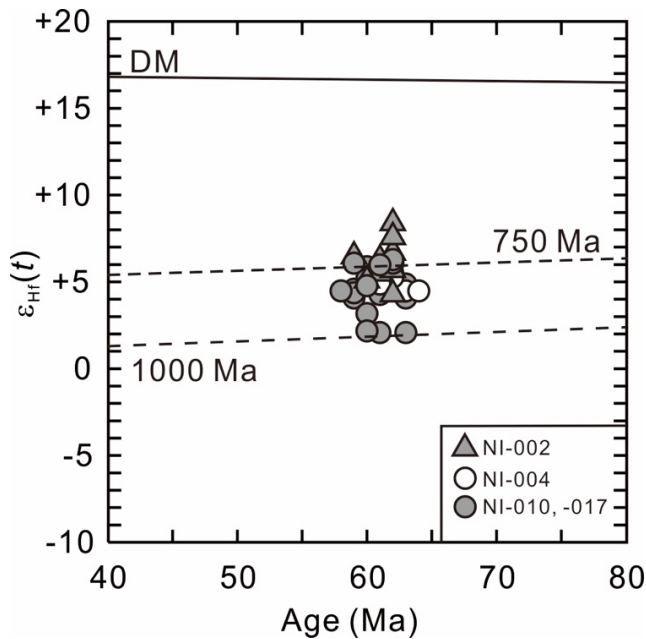


**Figure 6. Zircon Hf isotopic data from diorite and syenite of the North Island Complex.**

The evolution curves (dashed lines) at 1000 Ma and 750 Ma are calculated assuming Lu/Hf crustal value of 0.015 (Chauvel et al., 2008; Griffin et al., 2004). DM = depleted mantle.

### 5.3. ZIRCON HF ISOTOPES

Hafnium isotopes were analyzed on the same spot locations as reported for the U-Pb ages of samples NI-002, NI-004, NI-010, and NI-017 by Shellnutt et al. (2017). Not all zircons were analyzed for Hf isotopes because of the limited amount of material remaining after the initial session of ablation for geochronology. The initial ratios and  $\epsilon_{\text{Hf}}(t)$  values of the zircons were calculated on the basis of their individual U-Pb age. The complete dataset is in supplementary table S4 and the depleted mantle evolution and crust evolution curves in figure 6 are defined using present-day  $^{176}\text{Hf}/^{177}\text{Hf} = 0.28325$  and  $^{176}\text{Lu}/^{177}\text{Hf} = 0.0384$  (Griffin et al., 2000).

Nine zircons from NI-002 (diorite) yielded initial  $^{176}\text{Hf}/^{177}\text{Hf}(t)$  ratios from 0.282855 to 0.282970 with  $\epsilon_{\text{Hf}}(t)$  values ranging from +4.3 to +8.4. The  $T_{\text{DM1}}$  ages range from 402 Ma to 558 Ma whereas the  $T_{\text{DM2}}$  ages range from 598 Ma to 859 Ma. Five zircons from sample NI-004 (syenite) have initial  $^{176}\text{Hf}/^{177}\text{Hf}(t)$  ratios that range from 0.282859 to 0.282903 with  $\epsilon_{\text{Hf}}(t)$  values ranging from +4.5 to +6.0. The  $T_{\text{DM1}}$  ages range from 505 Ma to 569 Ma whereas the  $T_{\text{DM2}}$  ages range from 752 Ma to 849 Ma. Sample NI-010 (syenite) has the most analyses (19) and yielded initial  $^{176}\text{Hf}/^{177}\text{Hf}(t)$  ratios from 0.282792 to 0.282905 with  $\epsilon_{\text{Hf}}(t)$  values ranging from +2.1 to +6.1. The  $T_{\text{DM1}}$  ages range from 489 Ma to 655 Ma whereas the  $T_{\text{DM2}}$  ages range from 746 Ma to 1002 Ma. Six zircons from NI-017 (syenite) yielded initial  $^{176}\text{Hf}/^{177}\text{Hf}(t)$  ratios from 0.282797 to 0.282913 with  $\epsilon_{\text{Hf}}(t)$  values ranging from +2.2 to +6.3. The  $T_{\text{DM1}}$  ages

range from 487 Ma to 659 Ma whereas the  $T_{\text{DM2}}$  ages range from 729 Ma to 992 Ma.

### 5.4. MAJOR AND TRACE ELEMENTAL COMPOSITIONS

The rocks collected for this study include syenite ( $\text{SiO}_2 = 61\text{--}65$  wt%), one microsyenite ( $\text{SiO}_2 = \sim 70$  wt%) rock, and two diorites ( $\text{SiO}_2 \approx 57$  wt%) (fig. 7A). The alumina saturation index values show that all but one of the syenitic rocks are metaluminous (mol.  $\text{Al}_2\text{O}_3/\text{mol. CaO}+\text{Na}_2\text{O}+\text{K}_2\text{O} < 1$ ; mol.  $\text{Na}_2\text{O}+\text{K}_2\text{O}/\text{Al}_2\text{O}_3 < 1$ ) whereas the other is weakly (mol.  $\text{Na}_2\text{O}+\text{K}_2\text{O}/\text{Al}_2\text{O}_3 = 1.01$ ) peralkaline (fig. 7B). Most rocks are quartz, diopside, and hypersthene normative whereas two are wollastonite normative instead of hypersthene normative and two are olivine and nepheline normative. The dioritic rocks are olivine, nepheline and diopside normative. The concentration of MnO (i.e.,  $< 0.2$  wt%), MgO (i.e.,  $\leq 0.6$  wt%) and CaO (i.e.,  $< 2.1$  wt%) are low. All of the rocks have high  $\text{Fe}^*$  ( $\text{FeOt}/\text{MgO}+\text{FeOt} \geq 0.80$ ) values and classify as alkalic according to the modified alkali lime index scheme of B. R. Frost et al. (2001) (fig. 7C and D). The trace elemental characterization using the criteria of Eby (1992) and Whalen and Hildebrand (2019) shows the rocks to be similar to the A-type ( $A_1$ ) granitoids which is consistent with the major elemental classification scheme of B. R. Frost et al. (2001) (fig. 7E and F).

All of the rocks have uniformly low concentrations of transition metals with no distinction between the syenites, diorites, and microsyenite ( $\text{Sc} = 13\text{--}24$  ppm,  $\text{V} \leq 22$  ppm,  $\text{Cr} = 1\text{--}33$  ppm,  $\text{Co} \leq 9$  ppm,  $\text{Ni} = 1\text{--}96$  ppm,  $\text{Cu} \leq 10$  ppm,  $\text{Zn} = 44\text{--}128$  ppm). The large ion lithophile element (LILE) concentrations are more variable ( $\text{Rb} = 36.3\text{--}276$  ppm,  $\text{Sr} = 3\text{--}521$  ppm,  $\text{Cs} = 0.3\text{--}3.4$  ppm,  $\text{Ba} = 9\text{--}12170$  ppm). Sample NI-017 has the lowest Sr and Ba concentrations and the highest concentration of Rb. Overall, the concentration of Ba in all rocks is high with most samples having  $\sim 1300$  ppm whereas NI-002 has a value of 12170 ppm ( $\text{BaO} = \sim 1.3$  wt%). The high field strength elements (HFSE) are as equally variable as the LILE ( $\text{Zr} = 61\text{--}605$  ppm,  $\text{Nb} = 35\text{--}230$  ppm,  $\text{Y} = 13\text{--}57$  ppm,  $\text{Hf} = 1.36\text{--}13.6$  ppm,  $\text{Ta} = 1.83\text{--}16.1$  ppm,  $\text{Th} = 1.84\text{--}40.4$  ppm,  $\text{U} = 0.53\text{--}9.49$  ppm), but the microsyenite has the highest concentrations of incompatible elements. The primitive mantle normalized incompatible patterns of the rocks, for the exception of the microsyenite, are broadly similar although there is some variability in the Rb–Ba and Hf–Zr concentrations (fig. 8A and B). All rocks have similar light rare earth element enriched chondrite normalized rare earth element patterns with high  $\text{La}_\text{N}/\text{Sm}_\text{N}$  (4.7–13.0) and  $\text{La}_\text{N}/\text{Yb}_\text{N}$  (8.0–18.0) ratios (fig. 8C and D). Many of the samples have positive Eu-anomalies with  $\text{Eu}/\text{Eu}^*$  values [ $\text{Eu}_\text{N}/(\text{Sm}_\text{N} \times \text{Gd}_\text{N})^{0.5}$ ] ranging from 0.07 (NI-017) to 8.13 (NI-002) with most samples having values of 0.97–2.60.

### 5.5. SR AND ND ISOTOPES

Six samples were analyzed for Sr and Nd isotopes (table S6). The initial isotopic ratios of the rocks (diorite, syenite) were calculated based on their U-Pb ages from this and previous work. The initial  $^{87}\text{Sr}/^{86}\text{Sr}$  ratios range from 0.704095 to

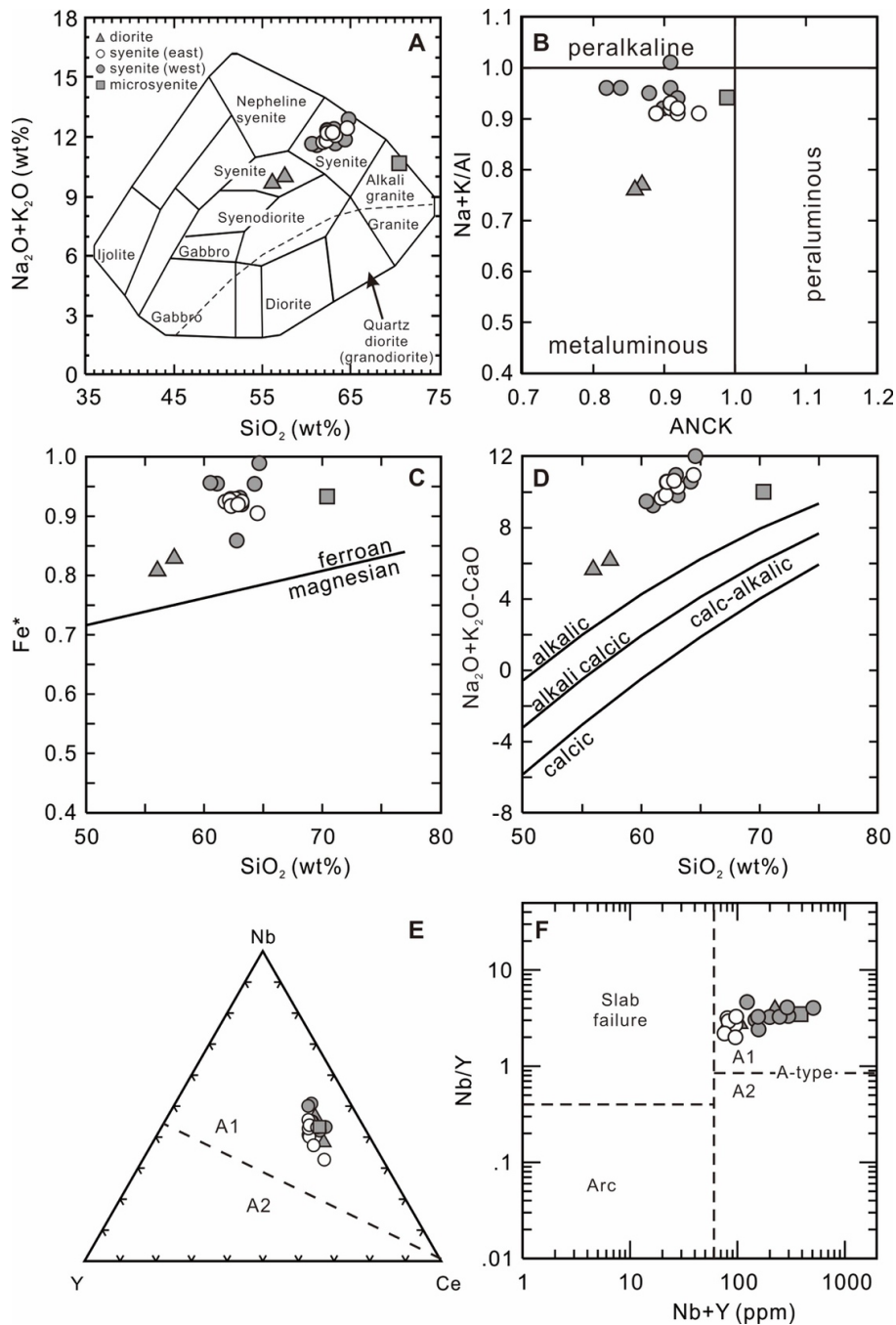


**Figure 7. Chemical classification of the rocks from the North Island complex.**

(A)  $\text{Na}_2\text{O}+\text{K}_2\text{O}$  (wt%) vs.  $\text{SiO}_2$  (wt%) classification of rocks (Cox et al., 1979). (B) Alkali index (mol.  $\text{Na}+\text{K}/\text{mol. Al}$ ) versus aluminum saturation index ( $\text{ASI} = \text{mol. Al}/\text{mol. Ca}+\text{Na}+\text{K}$ ). Classification of the NIC rocks using (C) the  $\text{Fe}^*$  [ $\text{FeO}^*/(\text{FeO}^*+\text{MgO})$ ] value and (D) the modified alkali-lime index ( $\text{Na}_2\text{O}+\text{K}_2\text{O}-\text{CaO}$ ) vs.  $\text{SiO}_2$  (wt%) of B. R. Frost et al. (2001). (E) Subdivision of A-type granitoids by Y-Nb-Ce into A<sub>1</sub>- and A<sub>2</sub>-subtypes (Eby, 1992). (F) Trace element discrimination of A-type granitic rocks of Whalen and Hildebrand (2019).

0.707533 with the dioritic sample having the highest value (0.707533) and the syenites with relatively uniform values (704095–0.704290). The initial  $^{143}\text{Nd}/^{144}\text{Nd}$  ratios are similar for all rocks and range from 0.512621 to 0.512659. The corresponding  $\epsilon_{\text{Nd}}(t)$  values, using  $^{147}\text{Sm}/^{144}\text{Nd}$  of 0.1967 and a  $\text{CHUR}_{\text{today}}$  value of 0.512638, are +1.2–+1.9 and fall within uncertainty ( $\pm 0.5$  epsilon units) of the analysis (fig. 9). The depleted mantle model ages ( $T_{\text{DM}}$ ) range from 658 Ma to 709 Ma.

## 6. DISCUSSION

### 6.1. PARENTAL MAGMA OF THE NORTH ISLAND PLUTONIC COMPLEX

The diorites, syenites, and microseynite of this study are ferroan, metaluminous, and alkalic according to the classification of B. R. Frost et al. (2001) and thus can be considered to be of similar character to the A-type granitoids (C. D. Frost & Frost, 2011). Furthermore, the biotite com-

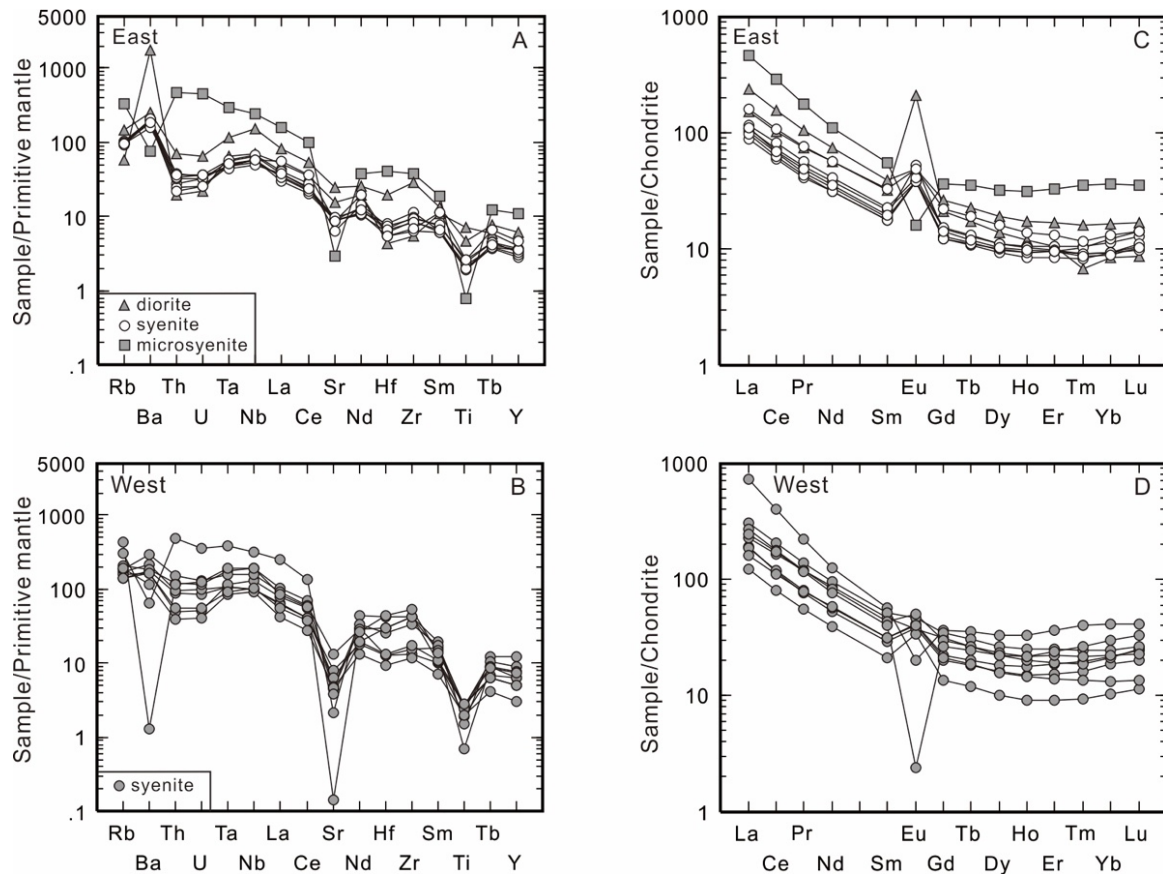


**Figure 8. (A) Primitive mantle normalized incompatible element and (B) chondrite normalized plots of the rocks (NI-001–NI-008) from eastern North Island (Congomont, Bernica). (C) Primitive mantle normalized incompatible element and (D) chondrite normalized plots of the rocks from western (NI-009–NI-017) North Island (Bernica, Mt. Des Cèdres). Normalizing values are from Sun and McDonough (1989).**

positions from the syenites are also consistent with A-type granitoids (fig. 10A and B). The within-plate or rift-related tectonic setting of the North Island Complex is not in dispute as they intruded Proterozoic basement rocks and the emplacement age (~63 Ma) is correlated to the rift-to-drift transition of the Seychelles microcontinental block from western India (Collier et al., 2008; Devey & Stephens, 1992; Ganerød et al., 2011; Shellnutt et al., 2017). However, A-type granitoids can be subdivided on the basis of their trace elemental chemistry and mineralogy into those derived from oceanic-island basalt-like magma and those derived from crustal sources (Abdel-Rahman, 1994; Bonin, 2007; Eby, 1992; Loiselle & Wones, 1979; Shabani et al., 2003; Whalen & Hildebrand, 2019).

The high field strength trace elemental classification plots of Eby (1992) and Whalen and Hildebrand (2019) and the biotite chemistry show the North Island rocks to be of the A<sub>1</sub>-sub-type (figs. 7E, F, and 10), that is, derived from an oceanic-island basalt (OIB)-like parental magma with minimal or no contamination from crustal material (i.e., melt or fluids). The role of crustal contamination in the North Island Complex will be addressed later, but is clear from the Sr-Nd-Hf isotopic data, the low Th/Nb<sub>PM</sub> (< 2) ratios, and lack of primitive mantle normalized negative Nb-Ta anomalies that the rocks were not principally derived from the continental crust. Moreover, the metalumi-

nous bulk rock compositions and presence of Ca-rich mafic minerals (e.g., hornblende, hedenbergite) demonstrate that the North Island syenites evolved differently from the ferroan, peralkaline, and alkalic granitoids as they contain alkali mafic silicate minerals (i.e., riebeckite-arfvedsonite, aegirine). Nevertheless, we can conclude that the likely composition of the parental magma of the NIC was similar to OIB.

## 6.2. MAGMATIC CONDITIONS OF THE NORTH ISLAND SYENITE COMPLEX

The magmatic conditions (temperature, redox state, pressure, volatile content) of the North Island syenites are constrained using mineral chemistry, mineral textures, and whole rock geochemical data. The geological relationship with the country rock is unknown as it is not exposed, but Late Paleozoic to Early Cenozoic sedimentary rocks are reported from oil exploration drill wells to the west and northeast of North Island suggesting that the rocks were emplaced within the upper crust (P. S. Plummer & Belle, 1995).

Magmatic temperatures of the North Island syenites are constrained using zircon saturation thermometry, SiO<sub>2</sub> composition, and clinopyroxene-liquid equilibrium temperatures estimates (Boehnke et al., 2013; Duan et al.,

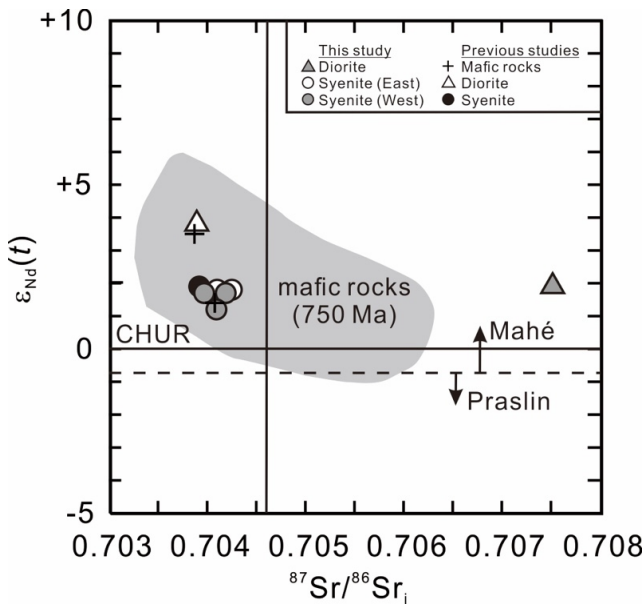


**Figure 9.** Sr-Nd isotopic data from the rocks of the North Island Complex.

Samples from this study have symbols as in figure 7. Additional data (symbols are in the upper right corner) from North Island are from Dickin et al. (1986) and Owen-Smith et al. (2013). Precambrian rock data (mafic rocks, Mahé, Praslin) compiled from Ashwal et al. (2002) and Shellnutt et al. (2020).

2022; France et al., 2010; Putirka, 2008). The zircon saturation [ $T_{Zr}(^{\circ}C)$ ] temperatures for the rocks with  $M$  ( $[Na+K+2Ca]/[Al*Si]$ ) values within the calibration range ( $M = 1.3$  to  $1.9$ ) of the calculation show significant variability  $688-872^{\circ}C$ , but there are two distinct groups. Samples NI-004V, NI-011, and NI-017 have the highest temperatures ( $849-872^{\circ}C$ ) whereas samples NI-003, NI-005, NI-007, NI-008, and NI-015 are  $\sim 100^{\circ}C$  lower ( $688-737^{\circ}C$ ).

The T-Si temperatures for all samples is  $726-930^{\circ}C$  with the microsyenite sample (NI-004V) having the lowest temperature ( $726^{\circ}C$ ), the diorites having the highest temperatures ( $909-930^{\circ}C$ ), and the syenite temperatures clustering at  $808-866^{\circ}C$ . Although there is overlap between the  $T_{Zr}(^{\circ}C)$  and T-Si temperature estimates, the T-Si results are generally higher. In comparison, the clinopyroxene-liquid equilibrium temperatures were calculated for sample NI-009 and yielded temperatures of  $837^{\circ}C$ ,  $844^{\circ}C$ , and  $866^{\circ}C$  and similar to the syenitic T-Si estimates and the highest  $T_{Zr}(^{\circ}C)$  estimates. It is likely that clinopyroxene is the liquidus or near liquidus mineral and thus closer to the initial magmatic temperature. The Al-in-clinopyroxene thermometer ( $T = 93.2Al_2O_3 + 742 [\pm 40^{\circ}C]$ ) yielded similar temperatures as the clinopyroxene-liquid equilibrium estimates and range from  $801^{\circ}C$  to  $839^{\circ}C$  for all samples (France et al., 2010). The highest temperature estimates are consistent between the three different methods and we conclude that the magmatic temperature of the syenitic rocks was likely  $800-900^{\circ}C$  and extended above  $900^{\circ}C$  for the diorites.

The emplacement depth was calculated from the clinopyroxene-based geobarometer of Putirka (2008). The equilibrium clinopyroxene-liquid temperatures of  $837^{\circ}C$ ,  $844^{\circ}C$ , and  $866^{\circ}C$  correspond to pressures of  $0.36$  GPa,  $0.33$  GPa, and  $0.34$  GPa (table S7). Assuming  $0.1$  GPa =  $3.7$  km then the depth of clinopyroxene crystallization was  $12-14$  km. We also apply the titanite barometer for granitic rocks of Erdmann et al. (2019). The results yielded pressures of  $0.19$  to  $0.27 \pm 0.1$  GPa ( $7-10$  km). We think that the titanite barometer estimates are meaningful as the compositions used to calibrate the equation include ferroan and met-aluminous granitic rocks and a mineral assemblage (i.e., amphibole-titanite-biotite-plagioclase-K-feldspar-quartz-magnetite $\pm$ ilmenite) similar to the North Island syenites. The  $0.06-0.17$  GPa difference between the clinopyroxene and titanite estimates are within uncertainty of each calcu-

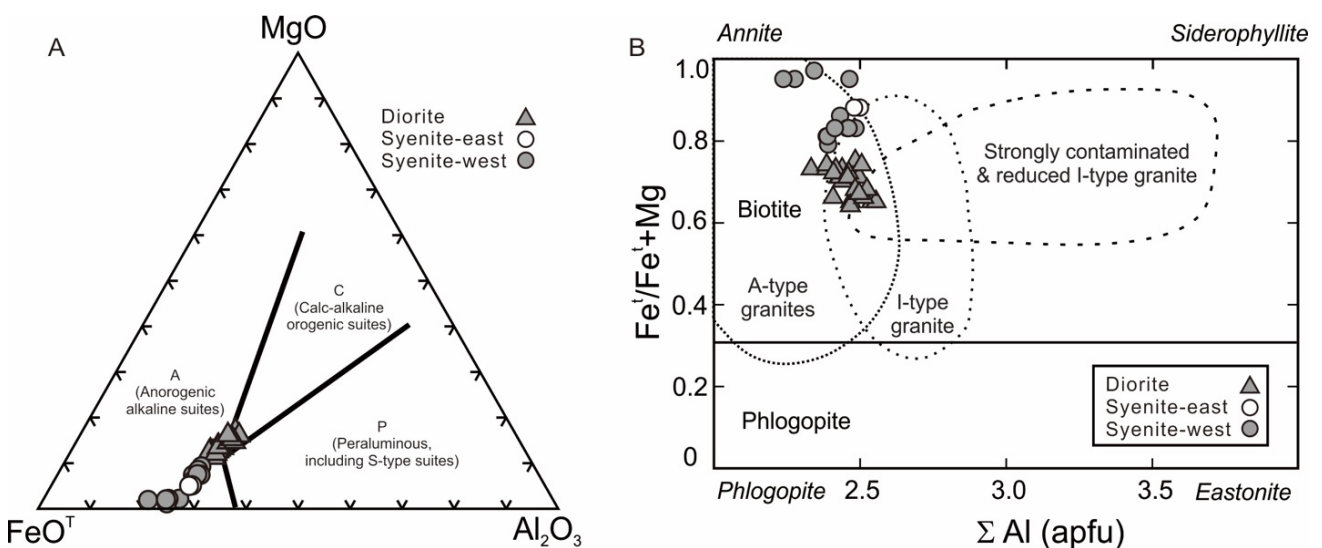


**Figure 10.** (A) Classification of biotite using the FeO-MgO- $Al_2O_3$  discrimination of Abdel-Rahman (1994). (B) The classification scheme and discrimination fields of biotite using  $Fe/(Fe+Mg)$  vs.  $\Sigma Al$  (apfu) are from Shabani et al. (2003).

lation but is possible that titanite crystallized later than the clinopyroxene and that the magma crystallized over a range of pressure (0.20–0.35 GPa) before reaching neutral buoyancy in the crust.

The relative oxidation state of the syenites is estimated using biotite mineral chemistry and ilmenite and magnetite pairs (Andersen et al., 1993; Shabani et al., 2003). Equation (1) is used to calculate the oxygen fugacity estimate of Eugster and Wones (1962) for biotite. It is based upon the  $\text{Fe}^{2+}$ - $\text{Fe}^{3+}$ - $\text{Mg}^{2+}$  composition of biotite, and the P and T for various oxygen buffers and defined as:

$$\text{Log}f_{\text{O}_2} = -\frac{A}{T} + B + \frac{C(P-1)}{T} \quad (1)$$

Where T is the temperature in Kelvin, P is the pressure in bar, and A, B, and C are oxygen fugacity buffer coefficients. The  $f_{\text{O}_2}$  calculation is dependent upon the coefficient (A, B, and C) values (Eugster & Wones, 1962). The coefficients are chosen based on the proportions of  $\text{Fe}^{2+}$ ,  $\text{Fe}^{3+}$ , and  $\text{Mg}^{2+}$  in biotite, which for this study are calculated using the program Fe23 (Nenova, 1997). The fayalite-magnetite-quartz (FMQ), Ni-NiO (NNO), and hematite-magnetite (HM) buffers are arranged in  $\text{Fe}^{2+}$ - $\text{Fe}^{3+}$ - $\text{Mg}^{2+}$  space and show the biotites fall along the FMQ buffer. For the redox estimates we used pressure equal to 0.3 GPa (3000 bar) and calculated the biotite temperatures using the method of Luhr et al. (1984). The results indicate that the biotite crystallized at  $\text{log}f_{\text{O}_2}$  values from -15.1 to -19.8 which correspond to  $\Delta\text{FMQ}$  values of -0.56 to -0.95 and indicate reducing to slightly reducing conditions (table S1). Furthermore, the ilmenite, magnetite, and clinopyroxene mineral chemistry provided additional constraints on the redox conditions using QUIF (Andersen et al., 1993). Trial values, that is those allowed to vary to find equilibrium, of temperature (1000 °C) and initial  $\text{log}f_{\text{O}_2}$  values ( $\text{log}f_{\text{O}_2} = -10$ ) were entered at a pressure of 0.3 GPa (3000 bar). The results of the calculations for samples NI-002, NI-003, NI-007, and NI-009 are in table S8. Samples NI-002 and NI-009 produce the highest temperatures (791 °C, 733 °C) and  $\text{log}f_{\text{O}_2}$  values (-15.21, -17.10) whereas NI-003 and NI-007 produced the lowest temperatures (562 °C, 609 °C) and  $\text{log}f_{\text{O}_2}$  values (-20.54, -18.53). We consider the results from NI-003 and NI-007 to be indicative of the subsolidus re-equilibration conditions rather than magmatic conditions as the temperatures are well below the expected solidus (600–650 °C) of the syenites. However, the temperature estimates from NI-002 and NI-009 approach the estimated magmatic range (i.e., 800–900°C) of the syenites and diorites and are probably closer to their crystallization conditions. If this is the case, then the redox conditions of the magnetite-ilmenite-clinopyroxene system crystallized under moderately reducing conditions ( $\Delta\text{FMQ} = -0.72$  to  $-1.28$ ) and similar to the redox conditions estimated from the biotite compositions.

The volatile (e.g.,  $\text{OH}^-$ ,  $\text{F}^-$ ,  $\text{Cl}^-$ ) concentration of the North Island syenites is poorly constrained. The presence of biotite, calcic amphibole, apatite, and titanite implies that the magma contained volatiles, but the whole rock loss on ignition values are low (0.34–0.85 wt%) and the rocks are mostly composed of hypersolvus (perthitic) alkali feldspar suggesting a relatively dry magma system (Martin & Bonin,

1976). Since magmatic carbonate and fluorine-rich minerals (e.g., bastnäsite, fluorite) were not observed in the rocks it is unlikely that the magma system was saturated in  $\text{CO}_2$ , and/or  $\text{F}_2$ . We can constrain the likely maximum water contents indirectly by using Rhyolite-MELTS to estimate the dry and water-rich liquidus temperatures and compare them to the clinopyroxene equilibrium, T-Si, and  $T_{\text{Zr}}$ (°C) temperatures. The dry liquidus temperatures at 0.3 GPa and  $\Delta\text{FMQ} = -1$  are 1110–1132 °C whereas if the LOI content is representative of the magma volatile content then liquidus temperatures under the same pressure and redox conditions is 1044–1099°C. The estimates are 150–300°C higher than the mineral and whole rock estimates. Water saturation for the syenites at 0.3 GPa and  $\Delta\text{FMQ} = -1$  using Rhyolite-MELTS is ~6 wt%, but it was discovered that the lowest water-rich liquidus temperatures occurred at 4.5 wt% water and ranged from 885 °C to 969 °C. The results suggest that the water-rich liquidus temperatures are within uncertainty of the clinopyroxene and whole rock temperature estimates indicating that the syenites may have contained up to 4.5 wt% water. If this was the case, then it is possible that the syenitic magma degassed a significant amount of water during emplacement and before significant crystallization the feldspars (cf., Shellnutt et al., 2022).

### 6.3. MAGMATIC DIFFERENTIATION OF THE NORTH ISLAND COMPLEX

The classification of the North Island syenites as an  $A_1$ -sub type implies that they are the products of mafic magma differentiation (Bonin, 2007; Eby, 1992; Loiseau & Wones, 1979). The whole rock and mineral chemical data indicate that the parental magma of the North Island syenites was OIB-like and the conditions under which the syenites formed were reducing to moderately oxidizing ( $\Delta\text{FMQ} = 0$  to  $-1$ ) and occurred at a pressure of 0.20–0.35 GPa.

Fractional crystallization modeling was carried out using Rhyolite-MELTS version 1.0.2 (Gualda et al., 2012) and a mafic starting composition similar to a gabbro (LA97N17A) reported from North Island by Owen-Smith et al. (2013). The parental composition used for the modeling is not primitive as the MgO (wt%) concentration (3.7 wt%) and Mg# (40) are low. Therefore, it is assumed that the parental magma for the model underwent a previous period of mafic silicate (e.g., olivine, clinopyroxene, orthopyroxene) crystal fractionation as it transited through the crust. The high concentration of Sr (770 ppm) and a positive chondrite normalized Eu-anomaly ( $\text{Eu}/\text{Eu}^* = 1.6$ ) of the parental composition is indicative of feldspar accumulation suggesting that plagioclase may have been crystallizing at the time of emplacement, but that it did not fractionate. We think that sample LA97N17A represents an earlier magmatic stage between the primary magma composition and the diorites as the highest plagioclase An value from the gabbro (An37) is higher than the highest value (An30) from the diorite (Owen-Smith et al., 2013). It is possible that the magma was at or close to water saturation based on the Rhyolite-MELTS liquidus temperature estimates. If this was the case, then it is possible that plagioclase crystallization was initially suppressed prior to magma emplacement which sub-

sequently enhanced feldspar accumulation (Pichavant & Macdonald, 2007; Sisson & Grove, 1993). The modeling redox and pressure conditions were set to  $\Delta\text{FMQ} = 0$  and  $-1$  and 0.3 GPa, and the initial water content of 1.5 wt% was selected as it is within the range of continental alkalic basalts but also higher than what would be expected for a primary OIB magma (Hauri, 2002; Liu et al., 2015). The modeling composition and conditions are summarized in table S9.

The liquid evolution curves of the  $\Delta\text{FMQ} = -1$  (white dots) and  $\Delta\text{FMQ} = 0$  (black dots) models are shown as Fenners diagrams in [figure 11](#). The complete modeling results and the crystallization assemblages can be found in online supplementary table S9. The liquid compositions are shown at 10 °C intervals and the starting temperature was set to 1300 °C. The liquidus temperature for the  $\Delta\text{FMQ} = -1$  model is 1200 °C when whitlockite crystallizes. The compositional range of the silicic system is generated from ~920 °C to ~800 °C. At 800 °C, ~83.5% of the total magma system crystallized with ~16.5% liquid remaining. The fractionated assemblage from the liquidus temperature to 800 °C is: whitlockite (1200–1130 °C), apatite (1120–800 °C), olivine (1110–850 °C), clinopyroxene (1110–1060 °C, 1040–1030 °C), spinel (1090–800 °C), plagioclase (1060–800 °C), alkali feldspar (890–800 °C), and biotite (850–800 °C). The proportions relative to the total solid and compositional ranges of the fractionated minerals at 800 °C are: whitlockite = 0.2%, apatite = 3.4%, olivine ( $\text{Fo}_{70-25}$ ) = 11.3%, clinopyroxene ( $\text{Wo}_{56-44}\text{En}_{30-36}\text{Fs}_{13-20}$ ) = 14.3%, spinel (titanomagnetite) = 8.5 wt%, plagioclase ( $\text{An}_{63-25}$ ) = 43.1%, alkali feldspar ( $\text{An}_{4-2}\text{Ab}_{37-32}\text{Or}_{59-66}$ ) = 19.2%, and biotite = 0.2%.

The liquidus temperature for the  $\Delta\text{FMQ} = 0$  model is 1120 °C as spinel and apatite crystallize. The compositional range of the silicic system is generated from ~920 °C to ~800 °C. At 800 °C, ~84% of the total magma system crystallized with ~16% liquid remaining. The fractionated assemblage from the liquidus temperature to 800 °C is: spinel (1120–770 °C), apatite (1120–770 °C), clinopyroxene (1100–1040 °C), plagioclase (1070–810 °C), olivine (1050–940 °C), ilmenite (940–800 °C), orthopyroxene (930 °C), biotite (920–800 °C), alkali feldspar (890–800 °C), and leucite (800 °C). The proportions, relative to the total solid, and compositional ranges of the fractionated minerals at 800 °C are: spinel (titanomagnetite) = 13.6%, apatite = 3.5%, clinopyroxene ( $\text{Wo}_{48-45}\text{En}_{37-40}\text{Fs}_{15}$ ) = 16.6%, plagioclase ( $\text{An}_{64-21}$ ) = 43.6%, olivine ( $\text{Fo}_{70-66}$ ) = 2.7%, ilmenite = 0.5%, orthopyroxene ( $\text{Mg}\# = 71$ ) = 0.2%, biotite = 1.2%, alkali feldspar ( $\text{An}_{4-2}\text{Ab}_{41-33}\text{Or}_{55-65}$ ) = 16.9%, and leucite = 1.1%.

The models show that the liquid evolution curves can reach the bulk composition of the syenitic rocks and pass through or closely to the dioritic rocks. The  $\Delta\text{FMQ} = -1$  is the better result as the primary difference between the models is the  $\text{Fe}_2\text{O}_3$  liquid evolution. The  $\Delta\text{FMQ} = 0$  model shows an earlier and greater reduction in  $\text{Fe}_2\text{O}_3$  and misses the intermediate compositions and the majority of the syenitic rocks. For both models, the bulk  $\text{Na}_2\text{O}$  concentration is slightly higher than that of the rocks, but the

modeled total alkalis ( $\text{Na}_2\text{O}+\text{K}_2\text{O}$ ) and  $\text{K}_2\text{O}$  concentration match well and the modeled alkali feldspar compositions ( $\text{An}_{4-2}\text{Ab}_{37-32}\text{Or}_{59-66}$ ) overlap with the majority of the measured alkali feldspar compositions ( $\text{An}_{4-1}\text{Ab}_{67-31}\text{Or}_{29-67}$ ) in the rocks. It is possible that the whole rock compositions are not exclusively a consequence of crystal fractionation and may involve crystal accumulation as the  $\text{Eu}/\text{Eu}^*$  values of many syenites are much greater than unity and the Ba concentrations (449–2071 ppm) can be high or very high (12170 ppm).

To examine the trace element evolution (Eu, Sm, and Gd) in the system we used MELTS (Smith & Asimow, 2005) and the same conditions and starting composition (LA97N-17A: Sm = 7.3 ppm; Eu = 3.9 ppm; Gd = 7.5 ppm) as the Rhyolite-MELTS models. The results are shown in [figure 12](#) and it is clear that the expected compositional evolution curve diverges from the data at higher  $\text{SiO}_2$  contents (table S10). The majority of samples show higher  $\text{Eu}/\text{Eu}^*$  values with a minority that fall along the model curve. The implication is that the high  $\text{Eu}/\text{Eu}^*$  values of the syenitic rocks are not expected and therefore, could be a consequence of feldspar accumulation. It is possible that crystal accumulation occurred fairly late in the crystallization history as the model shows that the divergence in  $\text{Eu}/\text{Eu}^*$  values does not occur until the liquid  $\text{SiO}_2$  composition reaches  $\geq 62$  wt.%, but the dioritic rocks also have  $\text{Eu}/\text{Eu}^*$  values greater than unity. Furthermore, the syenite samples located in the eastern portion of the island (Bernica, Congoment) tend to have higher  $\text{Eu}/\text{Eu}^*$  values (1.80–3.20) compared to those from the western portion (Grand'Anse, Mt. Des Cèdres) of the island ( $\text{Eu}/\text{Eu}^* = 0.44\text{--}2.03$ ). The compositional differences correlate with the rock textures as the rocks with the lowest  $\text{Eu}/\text{Eu}^*$  values (0.07–1.11) are medium grained (NI-011, -012, -013, -017). It could imply that the medium grained rocks are closer to the chilled margin and/or liquid composition of the intrusion. In spite of the uncertainty in the precise parental magma composition, we conclude that chemical differentiation of the North Island complex was primarily controlled by crystal fractionation under reducing conditions ( $\Delta\text{FMQ} = -1$ ) in the upper crust and that crystal accumulation of feldspar likely occurred during the formation of the gabbro, diorite, and most of the syenites. It is likely that the NIC was a closed or near-closed magma system.

#### 6.4. MAGMA SOURCE AND CRUSTAL CONTAMINATION

The parental magma of the North Island Complex was likely mafic and derived from a mantle source, but was unlikely to be from a depleted mantle source as mid-ocean ridge basalt tends to be tholeiitic rather than alkaline (or transitional) and has lower  $\text{TiO}_2$  (2.1–1.1 wt%) contents (Gale et al., 2013). The parental composition used for the modeling is a 'best guess' based on available data. The whole rock Sr-Nd-Hf isotopic values ( $I_{\text{Sr}} = 0.70387\text{--}0.70408$ ;  $\epsilon_{\text{Nd}}(t) = +1.4\text{--}+3.5$ ;  $\epsilon_{\text{Hf}}(t) = +0.8$ ), low Th/Nb<sub>PM</sub> (0.5–0.7) and high Nb/U (45–70) ratios, lack of a negative primitive mantle normalized Nb-Ta anomalies in LA97N17A and other mafic rocks of North Island suggest that they were derived from an oceanic hotspot source (Dickin et al., 1986; Owen-Smith

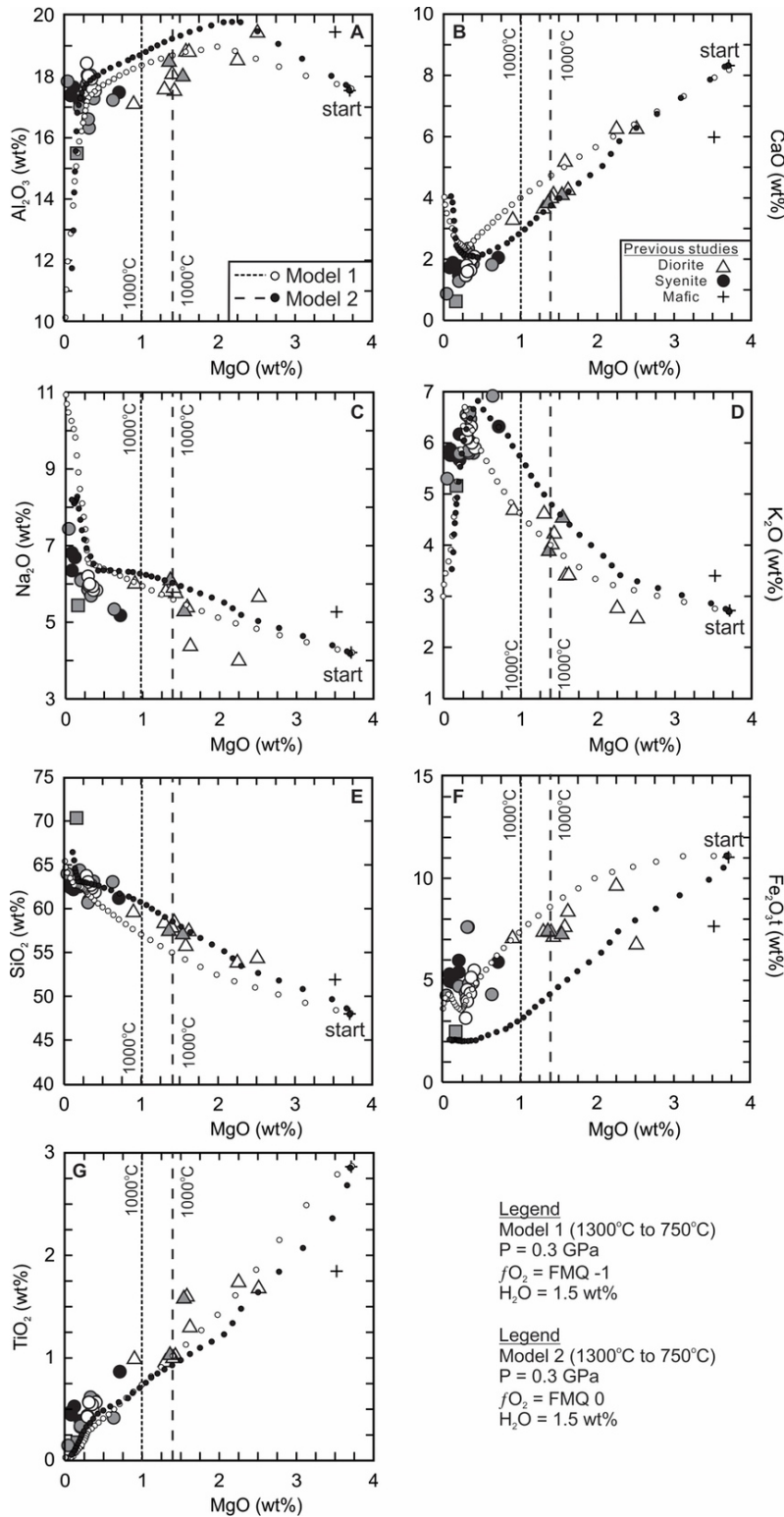


**Figure 11. The results of hydrous ( $\text{H}_2\text{O} = 1.5 \text{ wt}\%$ ) Rhyolite-MELTS fractional crystallization of the North Island Complex at 0.3 GPa and  $f_{\text{O}_2} = \Delta\text{FMQ} = -1$  (model 1) and  $\Delta\text{FMQ} = 0$  (model 2).**

(A)  $\text{Al}_2\text{O}_3$  (wt.%), (B) CaO (wt.%), (C)  $\text{Na}_2\text{O}$  (wt.%), (D)  $\text{K}_2\text{O}$  (wt.%), (E)  $\text{SiO}_2$  (wt.%), (F)  $\text{Fe}_2\text{O}_3\text{t}$  (wt.%), and (G)  $\text{TiO}_2$  (wt.%) vs. MgO (wt.%). The residual silicic liquids compositions are at 10 °C intervals. The complete modeling results are in online supplementary table S9. All data are normalized to 100%. The data symbols from this study are the same as in [figure 7](#). The symbols of additional data from Devey and Stephens (1992) and Owen-Smith et al. (2013) are shown in the lower-right corner of panel B.

et al., 2013). The isotopic and trace element ratios of the syenitic and dioritic rocks of North Island are within the

range of the mafic rocks ( $I_{\text{Sr}} = 0.70364\text{--}0.70429$ ;  $\varepsilon_{\text{Nd}}(t) = +1.4\text{--}+3.8$ ;  $\varepsilon_{\text{Hf}}(t) = +2.1\text{--}+8.4$ ,  $\text{Th}/\text{Nb}_{\text{PM}} = 0.3\text{--}1.6$ ; high



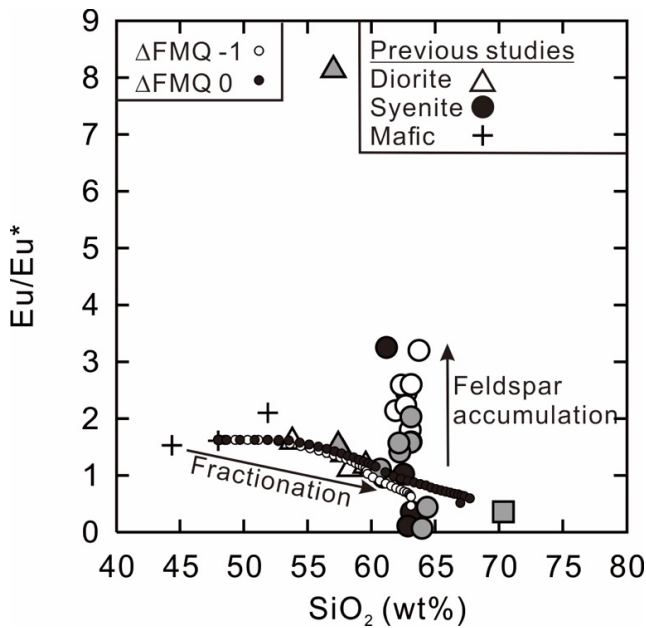


**Figure 12. Results of MELTS major ( $\text{SiO}_2$  wt%) and trace elemental (Sm, Eu, Gd) modeling using the same magmatic conditions and starting composition as the Rhyolite-MELTS modeling.**

Additional North Island data (symbols are in the upper right corner) from Devey and Stephens (1992) and Owen-Smith et al. (2013).

$\text{Nb}/\text{U} = 28\text{--}109$ ). The  $\text{Tb}/\text{Yb}_{\text{PM}}$  values of the North Island mafic rocks are 1.8 and 1.9 which are lower than the OIB composition of Sun and McDonough (1989) and places them within the range of basalts derived from the garnet-spinel transition zone (Wang et al., 2002).

An oceanic island/hotspot source of the parental magma is plausible as rifting of the Seychelles microcontinent from India is contemporaneous with the eruption of the Deccan Traps at  $\sim 65$  Ma (Basu et al., 1993; Pande, 2002; Schoene et al., 2015). The Deccan Traps are thought to be a consequence of melting of the Réunion hotspot although there is debate and alternative mantle sources are proposed (Glišović & Forte, 2017; Self et al., 2022). Nevertheless, geochemical evidence for crustal contamination from materials derived from the ancient basement of the Seychelles microcontinent in the North Island Complex is limited to non-existent and did not play a significant role in the genesis of the rocks. The only evidence of contamination in the North Island syenites is the presence of older zircons. Five zircons in sample NI-014 have  $^{238}\text{U}/^{206}\text{Pb}$  ages ranging from  $68 \pm 1$  Ma to  $73 \pm 1$  Ma whereas a single zircon from sample NI-003 was reported by Shellnutt et al. (2017) to have a  $^{238}\text{U}/^{206}\text{Pb}$  age of  $68 \pm 4$  Ma. These zircons are anomalous relative to the main zircon populations of the North Island rocks but are contemporaneous with ages reported from Deccan Traps-related rocks in western India and Pakistan and basaltic rocks reported from the western bank (Owen Bank A-1 and Seagull Shoals-1 wells) of the Seychelles microcontinent (Basu et al., 1993; Dongre et al., 2022; Kerr et al., 2010; Mahoney et al., 2002; Ph.S. Plum-

mer, 1995). The Deccan-related mineral and whole rock  $^{40}\text{Ar}/^{39}\text{Ar}$  ages range from  $68.17 \pm 1$  Ma to  $73.4 \pm 2.0$  Ma and are considered to be indicative of pre-flood basalt volcanic activity associated with the Réunion hotspot (Armitage et al., 2011; Kerr et al., 2010). The inherited zircons suggest that pre-flood basalt magmatic rocks may exist within the Seychelles microcontinent and that pre-Deccan magmatism should be present in the coastal regions of Gujarat and Maharashtra. The Sr-Nd isotopes of the  $\sim 70$  Ma basaltic rocks ( $^{87}\text{Sr}/^{86}\text{Sr}_i = 0.70382\text{--}0.70728$ ;  $\epsilon_{\text{Nd}}(t) = +2.6\text{--}+4.6$ ) reported by Mahoney et al. (2002) and Kerr et al. (2010) from Pakistan partially overlap with the North Island rocks. The reported basaltic rocks from Owen Bank and Seagull Shoals have whole rock K-Ar ages ranging from  $70.9 \pm 1.1$  Ma to  $77.6 \pm 1.0$  Ma, but little else is known (Ph.S. Plummer, 1995). The Sr-Nd isotopes ( $^{87}\text{Sr}/^{86}\text{Sr}_i = 0.70211\text{--}0.70309$ ;  $\epsilon_{\text{Nd}}(t) = +0.7\text{--}+3.2$ ) of the  $\sim 750$  Ma granites from the Mahé Group are also similar to the North Island rocks (Ashwal et al., 2002; Shellnutt et al., 2020). Thus, even if contamination of the North Island syenites by the  $\sim 70$  Ma or  $\sim 750$  Ma rocks occurred, it would be very difficult to confirm from an isotopic perspective. The single oldest inherited zircon reported from this study ( $95.9 \pm 6.6$  Ma) is contemporaneous with volcanism associated with the Marion hotspot and the rifting of Madagascar from India and also basalt ( $84 \pm 16$  Ma) dredged from the Amirante ridge,  $\sim 600$  km to the southwest of North Island (Ph.S. Plummer, 1995; Storey et al., 1995; Torsvik et al., 1998).

## 6.5. IMPLICATIONS FOR THE TECTONOMAGMATIC EVOLUTION OF THE NORTH ISLAND COMPLEX

The data and modeling presented in this study suggest that the parental magma of the North Island Complex was derived from the Réunion hotspot and emplaced into the continental lithosphere of the western India plate at  $\sim 63$  Ma. Initial crystallization of primitive mafic minerals likely occurred as the parental magma passed through the lower crust before reaching the upper crust. The resultant magma reached neutral buoyancy in the upper crust and continued to differentiate by fractional crystallization and feldspar accumulation. Contamination by crustal material was very limited or had a negligible influence on the evolution of the North Island Complex. Emplacement and differentiation of the parental magma occurred within a continental rift setting that eventually led to the separation of the Seychelles microcontinent from India and sea-floor spreading at the Carlsberg Ridge (Collier et al., 2008; Shellnutt et al., 2017).

The magmatic history of the North Island Complex is further revealed by the whole rock compositions and thermodynamic modeling. The syenitic rocks (NI-003 to NI-008) from the eastern part of North Island are chemically distinct from those of the western part (NI-009 to NI-017). For example, the eastern rocks tend to have lower incompatible element concentrations than the western rocks (fig. 13). Moreover, the eastern syenites tend to have higher Sr concentrations and  $\text{Eu}/\text{Eu}^*$  values than the western syenites. It is likely that the chemical differences are related to fractional crystallization as Ga, Rb, Y, Zr, Nb, REEs (except Eu), Hf, Ta, Th, and U are more incompatible and

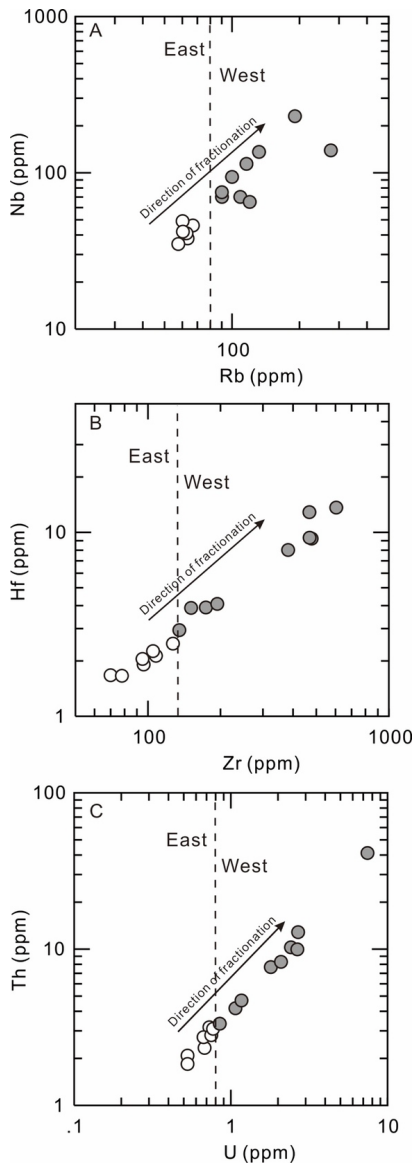


**Figure 13. A comparison of trace element compositions of the syenites from the eastern (NI-003–NI-008) and western (NI-009–NI-017) North Island complex.**

(A) Rb (ppm) vs. Nb (ppm), (B) Zr (ppm) vs. Hf (ppm), (C) U (ppm) vs. Th (ppm).

prefer to stay in the magma than partition into a mineral. Furthermore, the presence of the dioritic rocks in the east is unlikely to be happenstance as they represent the intermediate stage of the magma system. The low  $\text{Eu}/\text{Eu}^*$  values (0.44–0.97) of samples NI-011 and NI-012 are consistent with expectations of the MELTS trace element model in [figure 12](#) and were collected near the peak of Mt. Des Cèdres, the highest elevation of North Island. Therefore, it is possible that the elevated western portion of North Island represents the upper part of the magma chamber and is composed mostly of rocks derived from the fractionated magma with comparatively less accumulated feldspar ([fig. 14](#)).

Another implication of the study is for the general petrogenesis of metaluminous, ferroan, and alkalic A-type granites. C. D. Frost & B. R. Frost (C. D. Frost & Frost, 1997,

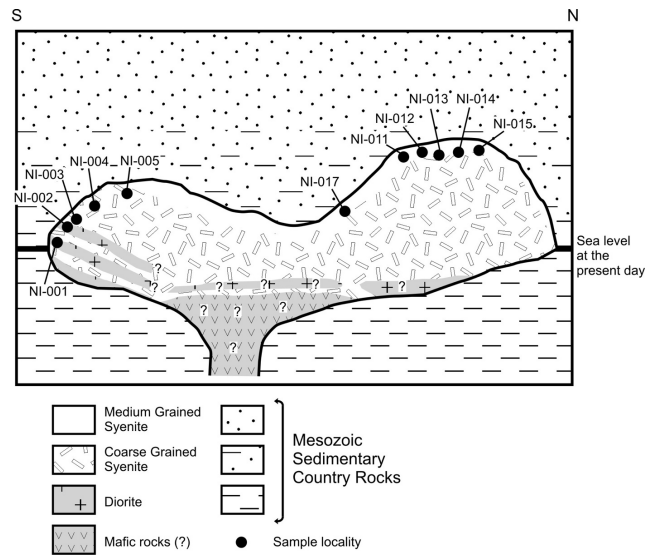


**Figure 14. Conceptual schematic model of the North Island Complex with approximate locations of some samples (Congomont = NI-001–NI-005; Mt. Des Cèdres = NI-011–NI-015) collected for this study.**

The lower parts of the intrusion are likely composed of mafic rocks that gradually become dioritic. It is uncertain (?) how extensive the mafic and dioritic rocks are. As the magma system evolved by fractional crystallization it became more syenitic. The differentiated syenitic magma rapidly cools against the upper contact with the Mesozoic country rock (P. S. Plummer & Belle, 1995) whereas the main body syenite cools slowly and accumulates alkali feldspar.

2011) suggest that the difference between the development of metaluminous and peralkaline quartz-bearing, ferroan, alkalic granitic rocks is the parental magma composition. For example, metaluminous ferroan, alkalic rocks are likely derived by differentiation of tholeiitic basalt whereas the peralkaline ferroan, alkalic rocks are derived by differentiation of transitional to alkali basalt. Moreover, pressure, relative oxidation state, and volatile content play important roles as to whether peralkaline or metaluminous silicic rocks are generated by mafic magma differentiation (C. D. Frost & Frost, 2011; Macdonald, 2012). In the case of the North Island Complex, it is unlikely that the parental magma was tholeiitic. The total alkali ( $\text{Na}_2\text{O}+\text{K}_2\text{O}$  wt%) content of the syenitic rocks of this study exceeds 11 wt%, the contemporaneous basaltic rocks reported from North Island and Silhouette are alkaline, and the most calcic plagioclase in the North Island gabbroic rocks is  $\text{An}_{37}$  which is common for the late crystallization stages of alkali basalt (Dickin et al., 1986; Greenough et al., 2005; Owen-Smith et al., 2013). Yet, the North Island Complex is metaluminous rather than peralkaline. The likely reason for the metaluminous character of the North Island syenites is their depth of differentiation rather than the parental composition or redox condition (e.g., Shellnutt, 2021).

The models presented in this study show that the initial feldspars crystallize after clinopyroxene and at 1060–1070 °C with a composition of  $\text{An}_{62.9-63.5}$  whereas changing the

model pressure to 0.1 GPa but maintaining the redox conditions and water content yielded feldspar compositions of  $An_{70.8-71.8}$  at 1060–1070 °C. The decrease in pressure causes a significant change in the An content (7–9 An units) of the feldspars. Furthermore, the duration and timing of clinopyroxene exerts an important influence. In our models, clinopyroxene crystallizes over a short duration (model 1 = 1110–1060 °C, 1040–1030 °C; model 2 = 1100–1040 °C) and only overlaps with plagioclase (model 1 = 1060–1030 °C; model 2 = 1070–1040 °C) for 30–40 °C. The early and ‘short’ period of clinopyroxene crystallization reduces the amount of available Ca in the magma without reducing Al. Consequently, the initial plagioclase will crystallize from a magma that is relatively depleted in Ca but enriched in Al. Since sodic plagioclase requires less Al to crystallize, due to the charge balance between  $Na^+$  and  $AlSi_3O_8^-$ , the ASI value will be relatively higher during magma crystallization. At lower pressure (0.1 GPa) the interval between initial plagioclase crystallization and clinopyroxene crystallization is 20 °C. Thus, the shorter interval between plagioclase and clinopyroxene crystallization cannot reduce as much Ca in the magma before the onset of plagioclase crystallization and the reduction of Al in the magma. Since calcic plagioclase requires more Al to crystallize due to the charge balance between  $Ca^{2+}$  and  $Al_2Si_2O_8^{2-}$ , the ASI value will be relatively lower during crystallization. Water acts to suppress the crystallization of feldspar (Pichavant & Macdonald, 2007; Sisson & Grove, 1993) and thus the water content of the original model ( $H_2O = 1.5$  wt%) will delay the crystallization of feldspar compared to models with lower water content. The higher water content and pressure will cause the crystallization of feldspar after clinopyroxene and at lower An values compared to low pressure and low water conditions. Models with similar redox conditions but lower water contents ( $H_2O = 0.5$  wt%) and different pressures (0.1 GPa vs. 0.3 GPa) crystallize feldspar at higher temperatures (1100–1130 °C), often before clinopyroxene, and yielded compositions that are different by only 2–5 An units rather 7–9 units at higher water contents. The lower water contents allow for earlier crystallization of relatively calcic feldspar as opposed to the higher water models. The implication of our modeling is that the residual magma will have higher alumina and thus evolve to metaluminous compositions rather than peralkaline compositions.

## 7. CONCLUSIONS

The North Island syenite complex was emplaced during the Early Paleogene (~63 Ma) and contemporaneous with the eruption of the youngest Deccan Traps. Magmatism was temporally associated with the rifting of the Seychelles microcontinent from the western margin of Peninsular India that was likely facilitated wholly or in part by the passage of the Indian plate over the Réunion hotspot. The mineral chemistry indicates that the syenitic magmas crystallized under reducing ( $\Delta FMQ = -1$ ) redox conditions at pressure typical of the upper crust (0.19 to 0.36 GPa). Whole rock and mineral equilibrium temperature estimates of the syenites consistently yielded maximum temperatures of

800–900 °C. Petrological modeling under the constraints determined by the mineral chemistry indicates that the North Island syenites were derived by hydrous fractional crystallization of an alkaline mafic parental magma. Feldspar accumulation likely occurred throughout the mafic-silicic crystallization history of the complex and is responsible for the positive chondrite normalized Eu-anomalies in some of the rocks. The syenites most affected by feldspar accumulation are located at Congoment and Bernica suggesting the magma system may have evolved from east to west (present position) in an upward trajectory and that the western most rocks are closer to the magma composition. Crustal contamination of the syenites by materials (melts, fluids) derived from the ancient Seychelles microcontinent basement could not be determined, although slightly older inherited zircons (68–73 Ma, ~95 Ma) were identified and testify to the existence of an older pre-flood basalt period of magmatism in the region prior to rifting. The dioritic rocks likely represent an intermediate stage of magma evolution from the original parental magma to the final syenitic rocks. The results of this study show that crystallization pressure can exert a significant influence on whether a ferroan A-type granitoid will be peralkaline or metaluminous.

## ACKNOWLEDGEMENTS

We are grateful to Mark Brandon, Trishya Owen-Smith, and Claire Bucholz for their constructive comments that helped to improve this manuscript. We thank and Javier Cotin, Elliott Mokhobo and the owners of North Island resort for their generous support for field work on North Island. Carol Cheung, Cynthia Tsai, and Robert Hsieh are thanked for their laboratory assistance. Funding support was provided by National Science and Technology Council (Taiwan) grant 112-2116-M-003-005-MY2 to JGS.

## AUTHOR CONTRIBUTIONS

JGS conceived of the study, collected samples, processed the data, and wrote the manuscript. TYL contributed to the writing of the manuscript. YI analyzed the mineral chemistry and contributed to the writing. HYL provide analytical expertise for the Hf isotopes and contributed the writing. CTP processed the biotite data. KS developed the *in situ* geochronology method and contributed to the writing.

## DATA AVAILABILITY

All data for this study are available at <https://doi.org/10.17632/8mkngdftfp.2>

Editor: Mark T. Brandon, Associate Editor: Claire Bucholz

Submitted: February 09, 2023 EDT, Accepted: February 22, 2024 EDT



This is an open-access article distributed under the terms of the Creative Commons Attribution 4.0 International License (CCBY-NC-ND-4.0). View this license's legal deed at <https://creativecommons.org/licenses/by-nc-nd/4.0> and legal code at <https://creativecommons.org/licenses/by-nc-nd/4.0/legalcode> for more information.

## REFERENCES

- Abdel-Rahman, A.-F. M. (1994). Nature of biotites from alkaline, calc-alkaline, and peraluminous magmas. *Journal of Petrology*, 35(2), 525–541. <https://doi.org/10.1093/ptrology/35.2.525>
- Andersen, D. J., Lindsley, D. H., & Davidson, P. M. (1993). QUILF: a PASCAL program to assess equilibria among Fe-Mg-Mn-Ti oxides, pyroxenes, olivine, and quartz. *Computers & Geosciences*, 19(9), 1333–1350. [https://doi.org/10.1016/0098-3004\(93\)90033-2](https://doi.org/10.1016/0098-3004(93)90033-2)
- Armitage, J. J., Collier, J. S., Minshull, T. A., & Henstock, T. J. (2011). Thin oceanic crust and flood basalts: India–Seychelles breakup. *Geochemistry, Geophysics, Geosystems*, 12(5). <https://doi.org/10.1029/2010gc003316>
- Ashwal, L. D. (2019). Wandering continents of the Indian Ocean. *South African Journal of Geology*, 122(4), 397–420. <https://doi.org/10.25131/sajg.122.0040>
- Ashwal, L. D., Demaiffe, D., & Torsvik, T. H. (2002). Petrogenesis of Neoproterozoic granitoids and related rocks from the Seychelles: the case for an Andean-type arc origin. *Journal of Petrology*, 43(1), 45–83. <https://doi.org/10.1093/ptrology/43.1.45>
- Baker, B. H. (1963). Geology and mineral resources of the Seychelles archipelago. *Geological Survey of Kenya Memoir*, 3, 140p.
- Baker, B. H., & Miller, J. A. (1963). Geology and geochronology of the Seychelles islands and structure of the floor of the Arabian Sea. *Nature*, 199(4891), 346–348. <https://doi.org/10.1038/199346a0>
- Basu, A. R., Renne, P. R., DasGupta, D. K., Teichmann, F., & Poreda, R. J. (1993). Early and Late Alkali Igneous Pulses and a High-<sup>3</sup>He Plume Origin for the Deccan Flood Basalts. *Science*, 261(5123), 902–906. <https://doi.org/10.1126/science.261.5123.902>
- Belousova, E. A., Griffin, W. L., O'Reilly, S. Y., & Fisher, N. I. (2002). Igneous zircon: trace element composition as an indicator of source rock type. *Contributions to Mineralogy and Petrology*, 143(5), 602–622. <https://doi.org/10.1007/s00410-002-0364-7>
- Blichert-Toft, J., & Albarède, F. (1997). The Lu-Hf isotope geochemistry of chondrites and the evolution of the mantle-crust system. *Earth and Planetary Science Letters*, 148(1–2), 243–258. [https://doi.org/10.1016/S0012-821X\(97\)00040-X](https://doi.org/10.1016/S0012-821X(97)00040-X)
- Boehnke, P., Watson, E. B., Trail, D., Harrison, T. M., & Schmitt, A. K. (2013). Zircon saturation re-revisited. *Chemical Geology*, 351, 324–334. <https://doi.org/10.1016/j.chemgeo.2013.05.028>
- Bonin, B. (2007). A-type granites and related rocks: evolution of a concept, problems and prospects. *Lithos*, 97(1–2), 1–29. <https://doi.org/10.1016/j.lithos.2006.12.007>
- Černý, P., Blevin, P. L., Cuney, M., & London, D. (2005). Granite-related ore deposits. In J. W. Hedenquist, J. F. H. Thompson, R. J. Goldfarb, & J. P. Richards (Eds.), *One Hundredth Anniversary Volume* (pp. 337–370). Society of Economic Geologists. <https://doi.org/10.5382/av100.12>
- Chakhmouradian, A. R., & Zaitsev, A. N. (2012). Rare earth mineralization in igneous rocks: Sources and processes. *Elements*, 8(5), 347–353. <https://doi.org/10.2113/gselements.8.5.347>
- Chauvel, C., Lewin, E., Carpentier, M., Arndt, N. T., & Marini, J.-C. (2008). Role of recycled oceanic basalt and sediment in generating the Hf–Nd mantle array. *Nature Geoscience*, 1(1), 64–67. <https://doi.org/10.1038/ngeo.2007.51>
- Clemens, J. D., Holloway, J. R., & White, A. J. R. (1986). Origin of an A-type granite. experimental constraints. *American Mineralogist*, 71(3–4), 317–324.
- Collier, J. S., Sansom, V., Ishizuka, O., Taylor, R. N., Minshull, T. A., & Whitmarsh, R. B. (2008). Age of Seychelles–India break-up. *Earth and Planetary Science Letters*, 272(1–2), 264–277. <https://doi.org/10.1016/j.epsl.2008.04.045>
- Collins, W. J., Beams, S. D., White, A. J. R., & Chappell, B. W. (1982). Nature and origin of A-type granites with particular reference to southeastern Australia. *Contributions to Mineralogy and Petrology*, 80(2), 189–200. <https://doi.org/10.1007/bf00374895>
- Corfu, F., Hanchar, J. M., Hoskin, P. W. O., & Kinny, P. (2003). Atlas of zircon textures. *Reviews in Mineralogy and Geochemistry*, 53(1), 468–500. <https://doi.org/10.2113/0530469>
- Cox, K. G., Bell, J. D., & Pankhurst, R. J. (1979). *The Interpretation of Igneous Rocks*. Springer Netherlands. <https://doi.org/10.1007/978-94-017-3373-1>

- Creaser, R. A., Grütter, H. S., Carlson, J., & Crawford, B. (2004). Macrocrystal phlogopite Rb–Sr dates for the Ekati property kimberlites: evidence for multiple intrusive episodes in the Paleocene and Eocene. *Lithos*, 76(1–4), 399–414. <https://doi.org/10.1016/j.lithos.2004.03.039>
- Dall'Agnol, R., Frost, C. D., & Rämö, O. T. (2012). IGCP Project 510 “A-type granites and related rocks through time”: project vita, results, and contribution to granite research. *Lithos*, 151, 1–16. <https://doi.org/10.1016/j.lithos.2012.08.003>
- Devey, C. W., & Stephens, W. E. (1992). Deccan-related magmatism west of the Seychelles-India rift. *Geological Society, London, Special Publications*, 68(1), 271–291. <https://doi.org/10.1144/gsl.sp.1992.068.01.17>
- Dickin, A. P., Fallick, A. E., Halliday, A. N., Macintyre, R. M., & Stephens, W. E. (1986). An isotopic and geochronological investigation of the younger igneous rocks of the Seychelles microcontinent. *Earth and Planetary Science Letters*, 81(1), 46–56. [https://doi.org/10.1016/0012-821x\(86\)90099-3](https://doi.org/10.1016/0012-821x(86)90099-3)
- Dongre, A., Dhote, P. S., Zamarkar, P., Sangode, S. J., Belyanin, G., Meshram, D. C., Patil, S. K., Karmakar, A., & Jain, L. (2022). Short-lived alkaline magmatism related to the Réunion plume in the Deccan Large Igneous Province: inferences from petrology,  $^{40}\text{Ar}/^{39}\text{Ar}$  geochronology and palaeomagnetism of lamprophyre from the Sarnu-Dandali Alkaline Igneous Complex. *Geological Society, London, Special Publications*, 513(1), 381–411. <https://doi.org/10.1144/sp513-2021-34>
- Dostal, J. (2017). Rare earth element deposits of alkaline igneous rocks. *Resources*, 6(3), 34. <https://doi.org/10.3390/resources6030034>
- Duan, M., Niu, Y., Sun, P., Chen, S., Kong, J., Li, J., Zhang, Y., Hu, Y., & Shao, F. (2022). A simple and robust method for calculating temperatures of granitoid magmas. *Mineralogy and Petrology*, 116(1), 93–103. <https://doi.org/10.1007/s00710-021-00769-5>
- Eby, G. N. (1990). The A-type granitoids: a review of their occurrence and chemical characteristics and speculations on their petrogenesis. *Lithos*, 26(1–2), 115–134. [https://doi.org/10.1016/0024-4937\(90\)90043-z](https://doi.org/10.1016/0024-4937(90)90043-z)
- Eby, G. N. (1992). Chemical subdivisions of the A-type granitoids: petrogenetic and tectonic implications. *Geology*, 20(7), 641–644. [https://doi.org/10.1130/0091-7613\(1992\)020<0641:CSOTAT>2.3.CO;2](https://doi.org/10.1130/0091-7613(1992)020<0641:CSOTAT>2.3.CO;2)
- Erdmann, S., Wang, R., Huang, F., Scaillet, B., Zhao, K., Liu, H., Chen, Y., & Faure, M. (2019). Titanite: a potential solidus barometer for granitic magma systems. *Comptes Rendus. Géoscience*, 351(8), 551–561. <https://doi.org/10.1016/j.crte.2019.09.002>
- Eugster, H. P., & Wones, D. R. (1962). Stability relations of the ferruginous biotite, annite. *Journal of Petrology*, 3(1), 82–125. <https://doi.org/10.1093/petrology/3.1.82>
- France, L., Koepke, J., Ildefonse, B., Cichy, S. B., & Deschamps, F. (2010). Hydrous partial melting in the sheeted dike complex at fast spreading ridges: experimental and natural observations. *Contributions to Mineralogy and Petrology*, 160(5), 683–704. <https://doi.org/10.1007/s00410-010-0502-6>
- Frost, B. R., Barnes, C. G., Collins, W. J., Arculus, R. J., Ellis, D. J., & Frost, C. D. (2001). A geochemical classification for granitic rocks. *Journal of Petrology*, 42(11), 2033–2048. <https://doi.org/10.1093/petrology/42.11.2033>
- Frost, C. D., & Frost, B. R. (1997). Reduced rapakivi-type granites: the tholeiite connection. *Geology*, 25(7), 647–650. [https://doi.org/10.1130/0091-7613\(1997\)025<0647:RRTGTT>2.3.CO;2](https://doi.org/10.1130/0091-7613(1997)025<0647:RRTGTT>2.3.CO;2)
- Frost, C. D., & Frost, B. R. (2011). On ferroan (A-type) granitoids: their compositional variability and modes of origin. *Journal of Petrology*, 52(1), 39–53. <https://doi.org/10.1093/petrology/egq070>
- Gaina, C., van Hinsbergen, D. J. J., & Spakman, W. (2015). Tectonic interactions between India and Arabia since the Jurassic reconstructed from marine geophysics, ophiolite geology, and seismic tomography. *Tectonics*, 34(5), 875–906. <https://doi.org/10.1002/2014tc003780>
- Gale, A., Dalton, C. A., Langmuir, C. H., Su, Y., & Schilling, J.-G. (2013). The mean composition of ocean ridge basalts. *Geochemistry, Geophysics, Geosystems*, 14(3), 489–518. <https://doi.org/10.1029/2012gc004334>
- Ganerød, M., Torsvik, T. H., van Hinsbergen, D. J. J., Gaina, C., Corfu, F., Werner, S., Owen-Smith, T. M., Ashwal, L. D., Webb, S. J., & Hendriks, B. W. H. (2011). Palaeoposition of the Seychelles microcontinent in relation to the Deccan Traps and the plume generation zone in Late Cretaceous–Early Palaeogene time. *Geological Society, London, Special Publications*, 357(1), 229–252. <https://doi.org/10.1144/sp357.12>
- Glišović, P., & Forte, A. M. (2017). On the deep-mantle origin of the Deccan Traps. *Science*, 355(6325), 613–616. <https://doi.org/10.1126/science.1254390>

- Greenough, J. D., Dostal, J., & Mallory-Greenough, L. M. (2005). Oceanic island volcanism I Mineralogy and Petrology. *Geoscience Canada*, 32(1), 29–45. <https://journals.lib.unb.ca/index.php/GC/article/view/2696>
- Griffin, W. L., Belousova, E. A., Shee, S. R., Pearson, N. J., & O'Reilly, S. Y. (2004). Archean crustal evolution in the northern Yilgarn Craton: U–Pb and Hf-isotope evidence from detrital zircons. *Precambrian Research*, 131(3–4), 231–282. <https://doi.org/10.1016/j.precamres.2003.12.011>
- Griffin, W. L., Pearson, N. J., Belousova, E. A., & Saeed, A. (2006). Comment: Hf-isotope heterogeneity in zircon 91500. *Chemical Geology*, 233(3–4), 358–363. <https://doi.org/10.1016/j.chemgeo.2006.03.007>
- Griffin, W. L., Pearson, N. J., Belousova, E., Jackson, S. E., van Achterbergh, E., O'Reilly, S. Y., & Shee, S. R. (2000). The Hf isotope composition of cratonic mantle: LAM-MC-ICPMS analysis of zircon megacrysts in kimberlites. *Geochimica et Cosmochimica Acta*, 64(1), 133–147. [https://doi.org/10.1016/s0016-7037\(99\)00343-9](https://doi.org/10.1016/s0016-7037(99)00343-9)
- Gualda, G. A. R., Ghiorso, M. S., Lemons, R. V., & Carley, T. L. (2012). Rhyolite-MELTS: a modified calibration of MELTS optimized for silica-rich, fluid-bearing magmatic systems. *Journal of Petrology*, 53(5), 875–890. <https://doi.org/10.1093/petrology/egr080>
- Hammond, J. O. S., Collier, J. S., Kendall, J.-M., Helffrich, G., & Rumpker, G. (2012). Plume scar in the mantle lithosphere beneath the Seychelles revealed by seismic imaging. *Earth and Planetary Science Letters*, 355–356(1), 20–31. <https://doi.org/10.1016/j.epsl.2012.08.020>
- Hammond, J. O. S., Kendall, J.-M., Collier, J. S., & Rumpker, G. (2013). The extent of continental crust beneath the Seychelles. *Earth and Planetary Science Letters*, 381(1), 166–176. <https://doi.org/10.1016/j.epsl.2013.08.023>
- Hattori, K., Sakata, S., Tanaka, M., Orihashi, Y., & Hirata, T. (2017). U–Pb age determination for zircons using laser ablation-ICP-mass spectrometry equipped with six multiple-ion counting detectors. *Journal of Analytical Atomic Spectrometry*, 32(1), 88–95. <https://doi.org/10.1039/c6ja00311g>
- Hauri, E. (2002). SIMS analysis of volatiles in silicate glasses, 2: isotopes and abundances in Hawaiian melt inclusions. *Chemical Geology*, 183(1–4), 115–141. [https://doi.org/10.1016/s0009-2541\(01\)00374-6](https://doi.org/10.1016/s0009-2541(01)00374-6)
- Hogan, J. P., Gilbert, M. C., & Weaver, B. L. (1992). A-types granites and rhyolites: Is A for ambiguous? *EOS, Transactions of the American Geophysical Union*, 73(47), 508. <https://doi.org/10.1029/91eo00372>
- Holmden, C., Creaser, R. A., & Muehlenbachs, K. (1997). Paleosalinities in ancient brackish water systems determined by <sup>87</sup>Sr/<sup>86</sup>Sr ratios in carbonate fossils: A case study from the Western Canada sedimentary basin. *Geochimica et Cosmochimica Acta*, 61(10), 2105–2118. [https://doi.org/10.1016/s0016-7037\(97\)00073-2](https://doi.org/10.1016/s0016-7037(97)00073-2)
- Horstwood, M. S. A., Košler, J., Gehrels, G., Jackson, S. E., McLean, N. M., Paton, C., Pearson, N. J., Sircombe, K., Sylvester, P., Vermeesch, P., Bowring, J. F., Condon, D. J., & Schoene, B. (2016). Community-derived standards for LA-ICP-MS U-(Th-)Pb geochronology – Uncertainty propagation, age interpretation and data reporting. *Geostandards and Geoanalytical Research*, 40(3), 311–332. <https://doi.org/10.1111/j.1751-908x.2016.00379.x>
- Hoskin, P. W. O., & Schaltegger, U. (2003). The composition of zircon and igneous and metamorphic petrogenesis. *Reviews in Mineralogy and Geochemistry*, 53(1), 27–62. <https://doi.org/10.2113/0530027>
- Kerr, A. C., Khan, M., Mahoney, J. J., Nicholson, K. N., & Hall, C. M. (2010). Late Cretaceous alkaline sills of the south Tethyan suture zone, Pakistan: initial melts of the Réunion hotspot? *Lithos*, 117(1–4), 161–171. <https://doi.org/10.1016/j.lithos.2010.02.010>
- Landenberger, B., & Collins, W. J. (1996). Derivation of A-type granites from a dehydrated charnockitic lower crust: evidence from the Chaelundi Complex, eastern Australia. *Journal of Petrology*, 37(1), 145–170. <https://doi.org/10.1093/petrology/37.1.145>
- Leake, B. E., Woolley, A. R., Arps, C. E. S., Birch, W. D., Gilbert, M. C., Grice, J. D., Hawthorne, F. C., Kato, A., Kisch, H. J., Krivovichev, V. G., Linthout, K., Laird, J., Mandarino, J. A., Maresch, W. V., Nickel, E. H., Schmacher, J. C., Smith, D. C., Stephenson, N. C. N., Ungaretti, L., & Gou, Y. (1997). Nomenclature of amphiboles: report of the subcommittee on amphiboles of the international mineralogical association, commission on new minerals and mineral names. *The Canadian Mineralogist*, 35(1), 219–246.
- Liu, J., Xia, Q.-K., Deloule, E., Ingrin, J., Chen, H., & Feng, M. (2015). Water content and oxygen isotopic composition of alkali basalts from the Taihang Mountains, China: recycled oceanic components in the mantle source. *Journal of Petrology*, 56(4), 681–702. <https://doi.org/10.1093/petrology/egv013>
- Loiselle, M. C., & Wones, D. R. (1979). Characteristics and origin of anorogenic granites. *Geological Society of America Abstracts with Programs*, 11, 468.
- Ludwig, K. R. (2012). *Isoplot v. 3.75: a geochronological toolkit for Microsoft Excel*. Berkeley Geochronology Center.

- Luhr, J. F., Carmichael, I. S. E., & Varekamp, J. C. (1984). The 1982 eruptions of El Chichón Volcano, Chiapas, Mexico: Mineralogy and petrology of the anhydrite-bearing pumices. *Journal of Volcanology and Geothermal Research*, 23(1–2), 69–108. [https://doi.org/10.1016/0377-0273\(84\)90057-x](https://doi.org/10.1016/0377-0273(84)90057-x)
- Macdonald, R. (2012). Evolution of peralkaline silicic complexes: lessons from the extrusive rocks. *Lithos*, 152(1), 11–22. <https://doi.org/10.1016/j.lithos.2012.01.014>
- Macdonald, R., Bagiński, B., Leat, P. T., White, J. C., & Dzierżanowski, P. (2011). Mineral stability in peralkaline silicic rocks: information from trachytes of the Menengai volcano, Kenya. *Lithos*, 125(1–2), 553–568. <https://doi.org/10.1016/j.lithos.2011.03.011>
- Mahoney, J. J., Duncan, R. A., Khan, W., Gnos, E., & McCormick, G. R. (2002). Cretaceous volcanic rocks of the South Tethyan suture zone, Pakistan: implications for the Réunion hotspot and Deccan Traps. *Earth and Planetary Science Letters*, 203(1), 295–310. [https://doi.org/10.1016/s0012-821x\(02\)00840-3](https://doi.org/10.1016/s0012-821x(02)00840-3)
- Martin, R. F., & Bonin, B. (1976). Water and magma genesis: the association hypersolvus granite–subsolvus granites. *The Canadian Mineralogist*, 14(3), 228–237.
- Nachit, H., Ibhi, A., Abia, E. H., & Ben Ohoud, M. (2005). Discrimination between primary magmatic biotites, reequilibrated biotites and neofomed biotites. *Comptes Rendus. Géoscience*, 337(16), 1415–1420. <https://doi.org/10.1016/j.crte.2005.09.002>
- Nenova, P. I. (1997). “Fe<sup>23</sup>”: A computer program for calculating the number of Fe<sup>+2</sup> and Fe<sup>+3</sup> ions in minerals. *Computers & Geosciences*, 23(2), 215–219. [https://doi.org/10.1016/s0098-3004\(97\)85445-3](https://doi.org/10.1016/s0098-3004(97)85445-3)
- Owen-Smith, T. M., Ashwal, L. D., Torsvik, T. H., Ganerød, M., Nebel, O., Webb, S. J., & Werner, S. C. (2013). Seychelles alkaline suite records the culmination of Deccan Traps continental flood volcanism. *Lithos*, 182–183(1), 33–47. <https://doi.org/10.1016/j.lithos.2013.09.011>
- Paces, J. B., & Miller, J. D. Jr. (1993). Precise U–Pb ages of Duluth Complex and related mafic intrusions, northeastern Minnesota: Geochronological insights to physical, petrogenetic, paleomagnetic, and tectonomagmatic processes associated with the 1.1 Ga Midcontinent Rift System. *Journal of Geophysical Research: Solid Earth*, 98(B8), 13997–14013. <https://doi.org/10.1029/93jb01159>
- Pande, K. (2002). Age and duration of the Deccan Traps, India: a review of radiometric and paleomagnetic constraints. *Proceedings of the Indian Academy of Science (Earth and Planetary Sciences)*, 111(2), 115–123. <https://doi.org/10.1007/BF2981139>
- Patiño Douce, A. E. (1997). Generation of metaluminous A-type granites by low-pressure melting of calc-alkaline granitoids. *Geology*, 25(8), 743–746. [https://doi.org/10.1130/0091-7613\(1997\)025<0743:GOMATG>2.3.CO;2](https://doi.org/10.1130/0091-7613(1997)025<0743:GOMATG>2.3.CO;2)
- Pichavant, M., & Macdonald, R. (2007). Crystallization of primitive basaltic magmas at crustal pressures and genesis of the calc-alkaline igneous suite: experimental evidence from St Vincent, Lesser Antilles arc. *Contributions to Mineralogy and Petrology*, 154(5), 535–558. <https://doi.org/10.1007/s00410-007-0208-6>
- Plummer, P. S., & Belle, E. R. (1995). Mesozoic tectono-stratigraphic evolution of the Seychelles microcontinent. *Sedimentary Geology*, 96(1–2), 73–91. [https://doi.org/10.1016/0037-0738\(94\)00127-g](https://doi.org/10.1016/0037-0738(94)00127-g)
- Plummer, Ph.S. (1995). Ages and geological significance of the igneous rocks from Seychelles. *Journal of African Earth Sciences*, 20(2), 91–101. [https://doi.org/10.1016/0899-5362\(95\)00035-r](https://doi.org/10.1016/0899-5362(95)00035-r)
- Putirka, K. D. (2008). Thermometers and barometers for volcanic systems. *Reviews in Mineralogy and Geochemistry*, 69(1), 61–120. <https://doi.org/10.2138/rmg.2008.69.3>
- Sakata, S., Hattori, K., Iwano, H., Yokoyama, T. D., Danhara, T., & Hirata, T. (2014). Determination of U–Pb ages for young zircons using laser ablation–ICP–mass spectrometry coupled with an ion detection attenuator device. *Geostandards and Geoanalytical Research*, 38(4), 409–420. <https://doi.org/10.1111/j.1751-908x.2014.00320.x>
- Schoene, B., Samperton, K. M., Eddy, M. P., Keller, G., Adatte, T., Bowring, S. A., Khadri, S. F. R., & Gertsch, B. (2015). U–Pb geochronology of the Deccan Traps and relation to the end-Cretaceous mass extinction. *Science*, 347(6218), 182–184. <https://doi.org/10.1126/science.aaa0118>
- Self, S., Mittal, T., Dole, G., & Vanderkluyzen, L. (2022). Toward understanding Deccan volcanism. *Annual Review of Earth and Planetary Sciences*, 50(1), 477–506. <https://doi.org/10.1146/annurev-earth-012721-051416>
- Shabani, A. A. T., Lalonde, A. E., & Whalen, J. B. (2003). Composition of biotite from granitic rocks of the Canadian Appalachian Orogen: a potential tectonomagmatic indicator? *The Canadian Mineralogist*, 41(6), 1381–1396. <https://doi.org/10.2137/gscanmin.41.6.1381>



- Shellnutt, J. G. (2021). A cumulate syenite in the upper part of the Hongge-layered mafic-ultramafic intrusion, Emeishan large igneous province, SW China. *International Journal of Earth Sciences*, 110(8), 2979–3000. <https://doi.org/10.1007/s00531-021-02096-8>
- Shellnutt, J. G., Iizuka, Y., Lee, T. Y., & Chen, W. Y. (2022). Mineral chemistry from the Late Cretaceous peralkaline rhyolite at Hadjer el Khamis, Chad: constraints on magmatic conditions. *Neues Jahrbuch Für Mineralogie Abhandlungen*, 198(1), 25–44. <https://doi.org/10.1127/njma/2022/0338>
- Shellnutt, J. G., Lee, T.-Y., Chiu, H.-Y., Lee, Y.-H., & Wong, J. (2015). Evidence of Middle Jurassic magmatism within the Seychelles microcontinent: implications for the breakup of Gondwana. *Geophysical Research Letters*, 42(23), 10207–10215. <https://doi.org/10.1002/2015gl066036>
- Shellnutt, J. G., Lee, T.-Y., Torng, P.-K., Yang, C.-C., & Lee, Y.-H. (2016). Late Cretaceous intraplate silicic volcanic in the Lake Chad region: a northern extension of the Cameroon volcanic line? *Geochemistry, Geophysics, Geosystems*, 17(7), 2803–2824. <https://doi.org/10.1002/2016gc006298>
- Shellnutt, J. G., Nguyen, T. D., & Lee, H.-Y. (2020). Resolving the origin of the Seychelles microcontinent: insight from zircon geochronology and Hf isotopes. *Precambrian Research*, 343(1), 105725. <https://doi.org/10.1016/j.precamres.2020.105725>
- Shellnutt, J. G., Wang, K.-L., Zellmer, G. F., Iizuka, Y., Jahn, B.-M., Pang, K.-N., Qi, L., & Zhou, M.-F. (2011). Three Fe-Ti oxide ore-bearing gabbro-granitoid complexes in the Panxi region of the Permian Emeishan large igneous province, SW China. *American Journal of Science*, 311(9), 773–812. <https://doi.org/10.2475/09.2011.02>
- Shellnutt, J. G., Yeh, M.-W., Suga, K., Lee, T.-Y., Lee, H.-Y., & Lin, T.-H. (2017). Temporal and structural evolution of the Early Palaeogene rocks of the Seychelles microcontinent. *Scientific Reports*, 7(1). <https://doi.org/10.1038/s41598-017-00248-y>
- Sisson, T. W., & Grove, T. L. (1993). Experimental investigations of the role of H<sub>2</sub>O in calc-alkaline differentiation and subduction zone magmatism. *Contributions to Mineralogy and Petrology*, 113(2), 143–166. <https://doi.org/10.1007/bf00283225>
- Sláma, J., Košler, J., Condon, D. J., Crowley, J. L., Gerdes, A., Hanchar, J. M., Horstwood, M. S. A., Morris, G. A., Nasdala, L., Norberg, N., Schaltegger, U., Schoene, B., Tubrett, M. N., & Whitehouse, M. J. (2008). Plešovice zircon — A new natural reference material for U–Pb and Hf isotopic microanalysis. *Chemical Geology*, 249(1–2), 1–35. <https://doi.org/10.1016/j.chemgeo.2007.11.005>
- Smith, P. M., & Asimow, P. D. (2005). Adibat\_1ph: a new public front-end to the MELTS, pMELTS, and pHMELTS models. *Geochemistry, Geophysics, Geosystems*, 6(2). <https://doi.org/10.1029/2004gc000816>
- Söderlund, U., Patchett, P. J., Vervoort, J. D., & Isachsen, C. E. (2004). The <sup>176</sup>Lu decay constant determined by Lu–Hf and U–Pb isotope systematics of Precambrian mafic intrusions. *Earth and Planetary Science Letters*, 219(3–4), 311–324. [https://doi.org/10.1016/s0012-821x\(04\)00012-3](https://doi.org/10.1016/s0012-821x(04)00012-3)
- Stacey, J. S., & Kramers, J. D. (1975). Approximation of terrestrial lead isotope evolution by a two-stage model. *Earth and Planetary Science Letters*, 26(2), 207–221. [https://doi.org/10.1016/0012-821x\(75\)90088-6](https://doi.org/10.1016/0012-821x(75)90088-6)
- Stephens, W. E. (1996). Geology of Silhouette Island. *Phelsuma*, 4, 11–18.
- Stern, R. A. (1997). The GSC sensitive high ion microprobe (SHRIMP): analytical techniques of zircon U–Th–Pb age determinations and performance evaluation. *Geological Survey of Canada Current Research, Radiogenic Age and Isotopic Studies Report*, 10, 1–32. <https://doi.org/10.4095/209089>
- Storey, M., Mahoney, J. J., Saunders, A. D., Duncan, R. A., Kelley, S. P., & Coffin, M. F. (1995). Timing of hot spot—related volcanism and the breakup of Madagascar and India. *Science*, 267(5199), 852–855. <https://doi.org/10.1126/science.267.5199.852>
- Sun, S. S., & McDonough, W. F. (1989). Chemical and isotopic systematics of oceanic basalts: implications for mantle composition and processes. *Geological Society, London, Special Publications*, 42(1), 313–345. <https://doi.org/10.1144/gsl.sp.1989.042.01.19>
- Tindle, A. G., & Webb, P. C. (1994). Probe-AMPH—A spreadsheet program to classify microprobe-derived amphibole analyses. *Computers & Geosciences*, 20(7–8), 1201–1228. [https://doi.org/10.1016/0098-3004\(94\)90071-x](https://doi.org/10.1016/0098-3004(94)90071-x)
- Tindle, Andrew G., & Webb, P. C. (1990). Estimation of lithium contents in trioctahedral micas using microprobe data: application to micas from granitic rocks. *European Journal of Mineralogy*, 2(5), 595–610. <https://doi.org/10.1127/ejm/2/5/0595>

- Torsvik, T. H., Amundsen, H., Hartz, E. H., Corfu, F., Kuzsnir, N., Gaina, C., Doubrovine, P. V., Steinberger, B., Ashwal, L. D., & Jamtveit, B. (2013). A Precambrian microcontinent in the Indian Ocean. *Nature Geoscience*, 6(3), 223–227. <https://doi.org/10.1038/ngeo1736>
- Torsvik, T. H., Tucker, R. D., Ashwal, L. D., Eide, E. A., Rakotosolofo, N. A., & de Wit, M. J. (1998). Late Cretaceous magmatism in Madagascar: palaeomagnetic evidence for a stationary Marion hotspot. *Earth and Planetary Science Letters*, 164(1–2), 221–232. [https://doi.org/10.1016/S0012-821X\(98\)00206-4](https://doi.org/10.1016/S0012-821X(98)00206-4)
- Tucker, R. D., Ashwal, L. D., & Torsvik, T. H. (2001). U–Pb geochronology of Seychelles granitoids: a Neoproterozoic continental arc fragment. *Earth and Planetary Science Letters*, 187(1–2), 27–38. [https://doi.org/10.1016/S0012-821X\(01\)00282-5](https://doi.org/10.1016/S0012-821X(01)00282-5)
- Wang, K., Plank, T., Walker, J. D., & Smith, E. I. (2002). A mantle melting profile across the Basin and Range, SW USA. *Journal of Geophysical Research: Solid Earth*, 107(B1). <https://doi.org/10.1029/2001jb000209>
- Weis, D., & Deutsch, S. (1984). Nd and Pb isotope evidence from the Seychelles granites and their xenoliths: mantle origin with slight upper-crust interaction for alkaline anorogenic complexes. *Isotope Geoscience*, 2(1), 13–35. [https://doi.org/10.1016/0009-2541\(84\)90163-3](https://doi.org/10.1016/0009-2541(84)90163-3)
- Whalen, J. B., & Hildebrand, R. S. (2019). Trace element discrimination of arc, slab failure, and A-type granitic rocks. *Lithos*, 348–349, 105179. <https://doi.org/10.1016/j.lithos.2019.105179>
- White, J. C., Parker, D. F., & Ren, M. (2009). The origin of trachyte and pantellerite from Pantelleria, Italy: insights from major element, trace element, and thermodynamic modelling. *Journal of Volcanology and Geothermal Research*, 179(1–2), 33–55. <https://doi.org/10.1016/j.jvolgeores.2008.10.007>
- Woodhead, J. D., & Hergt, J. M. (2005). A preliminary appraisal of seven natural zircon reference materials for in situ Hf isotope determination. *Geostandards and Geoanalytical Research*, 29(2), 183–195. <https://doi.org/10.1111/j.1751-908x.2005.tb00891.x>
- Woods, G. (2017). Lead isotope analysis: removal of 204Hg isobaric interference on 204Pb using ICP-QQQ MS/MS reaction cell. In *Handbook of ICP-QQQ Applications using the Agilent 8800 and 8900* (3rd ed.).
- Wu, F.-Y., Yang, Y.-H., Xie, L.-W., Yang, J.-H., & Xu, P. (2006). Hf isotopic compositions of the standard zircons and baddeleyites used in U–Pb geochronology. *Chemical Geology*, 234(1–2), 105–126. <https://doi.org/10.1016/j.chemgeo.2006.05.003>

## SUPPLEMENTARY MATERIALS

### Supplementary material, Table S1

Download: <https://ajsonline.org/article/94773-petrogenesis-of-the-early-paleogene-north-island-syenite-complex-seychelles/attachment/199203.xlsx>

---

### Supplementary material, Table S2

Download: <https://ajsonline.org/article/94773-petrogenesis-of-the-early-paleogene-north-island-syenite-complex-seychelles/attachment/199204.docx>

---

### Supplementary material, Table S3

Download: <https://ajsonline.org/article/94773-petrogenesis-of-the-early-paleogene-north-island-syenite-complex-seychelles/attachment/199202.xlsx>

---

### Supplementary material, Table S4

Download: <https://ajsonline.org/article/94773-petrogenesis-of-the-early-paleogene-north-island-syenite-complex-seychelles/attachment/199201.xls>

---

### Supplementary material, Table S5

Download: <https://ajsonline.org/article/94773-petrogenesis-of-the-early-paleogene-north-island-syenite-complex-seychelles/attachment/199200.docx>

---

### Supplementary material, Table S6

Download: <https://ajsonline.org/article/94773-petrogenesis-of-the-early-paleogene-north-island-syenite-complex-seychelles/attachment/199199.docx>

---

### Supplementary material, Table S7

Download: <https://ajsonline.org/article/94773-petrogenesis-of-the-early-paleogene-north-island-syenite-complex-seychelles/attachment/199197.xls>

---

### Supplementary material, Table S8

Download: <https://ajsonline.org/article/94773-petrogenesis-of-the-early-paleogene-north-island-syenite-complex-seychelles/attachment/199198.xlsx>

---

### Supplementary material, Table S9

Download: <https://ajsonline.org/article/94773-petrogenesis-of-the-early-paleogene-north-island-syenite-complex-seychelles/attachment/199209.xlsx>

---

## **Supplementary material, Table S10**

Download: <https://ajsonline.org/article/94773-petrogenesis-of-the-early-paleogene-north-island-syenite-complex-seychelles/attachment/199208.xlsx>

---

## **Supplementary material, Figures S1 and S2**

Download: <https://ajsonline.org/article/94773-petrogenesis-of-the-early-paleogene-north-island-syenite-complex-seychelles/attachment/199205.docx>

---

## **Supplementary Materials, Methods**

Download: <https://ajsonline.org/article/94773-petrogenesis-of-the-early-paleogene-north-island-syenite-complex-seychelles/attachment/199207.docx>

---

## **Supplementary Materials, Data**

Download: <https://ajsonline.org/article/94773-petrogenesis-of-the-early-paleogene-north-island-syenite-complex-seychelles/attachment/199206.xlsx>

---